Electron-impact excitation of the $n\ ^1P$ levels of helium: Theory and experiment

David C. Cartwright and George Csanak
University of California, Los Alamos National Laboratory, Los Alamos, New Mexico 87545

Sandor Trajmar and D. F. Register*
Jet Propulsion Laboratory, California Institute of Technology, Pasedena, California 91109
(Received 26 December 1990)

New experimental electron-energy-loss data have been used to extract differential and integral cross sections for excitation of the $2\ ^1P$ level, and for the overlapping ($3\ ^1P, 3\ ^1D, 3\ ^3D$) levels of helium, at 30-, 50-, and 100-eV incident electron energies. First-order many-body theory (FOMBT) has been used to calculate the differential and integral cross sections for excitation of the $n\ ^1P$ ($n=2,\ldots,6$) levels of helium by electron impact, for incident electron energies from threshold to 500 eV. Detailed comparisons between these two new sets of data are made as well as comparisons with appropriate published experimental and theoretical results. A simple scaling relationship is derived from the FOMBT results for $n=2,\ldots,6$ that provides differential and integral cross sections for all symmetry final levels of helium with $n \geq 6$.

PACS number(s): 34.80.Dp

I. INTRODUCTION

Electron-impact excitation of helium represents one of the simplest inelastic electron-collision processes that can be easily studied both theoretically and experimentally and, therefore, is of great interest from a basic collision-physics point of view. Because helium is one of the most abundant elements in the universe, and its emission and absorption lines are observed in a wide variety of stellar objects, the study of electron-impact excitation of helium is also of interest in astrophysics. The $1\ ^1S \rightarrow n\ ^1P$ excitation cross sections are especially important because emissions from the $n\ ^1P$ ($n=2,3,..$) levels are a dominant feature in helium emission spectra.

Electron-impact excitation of the $n\ ^1P$ ($n=2,3,\ldots$) levels of helium was one of the first problems studied both experimentally and theoretically. In 1931, Massey and Mohr [1] reported theoretical Born-Oppenheimer approximation results for excitation of several levels of helium, including the $2\ ^1P$ and $3\ ^1P$ levels, and compared their results with the available optical excitation functions [2] and with high-energy differential-cross-section (DCS) data [3]. The first low-energy ($E \leq 50$ eV) electron-impact DCS measurement was performed in 1932 by Mohr and Nicoll [4], who reported results at several incident electron energies for $2\ ^1P$ excitation. Subsequently, Massey and Mohr carried out the first distorted-wave-approximation (DWA) cross-section calculations for excitation of the $2\ ^1P$ and $2\ ^3P$ levels [5] and also reported results from the Born approximation for excitation of the $n\ ^1P$ ($n=2-5$) levels [6]. In this latter paper, in conjunction with the experiment of Mohr and Nicoll [4], these authors commented that the angular distributions of scattered electrons of the same incident velocity that have excited the $2\ ^1P$ and $3\ ^1P$ levels of helium are nearly identical when fitted together at one angle, as predicted by theory. This observation was confirmed, and further developed, some 55 years later by two of the present authors [7,8] and will be discussed in the present paper. The early theoretical and experimental work was well summarized by Bates *et al.* [9,10].

Since these pioneering studies, extensive theoretical results, a number of experimental integral cross-section (ICS) results, but only very limited experiment DCS results, have been reported for excitation of the $n\ ^1P$ ($n=2,3,\ldots$) levels. We call attention to the accurate Born-approximation results of Kim and Inokuti [11], the differential and integral cross section studies of Truhlar *et al.* [12], and the DWA studies of Madison and Shelton [13]. In the latter work, detailed studies on excitation of the $2\ ^1P$ level with various DWA schemes were compared with each other and with available experimental data. The results of both theoretical and experimental investigations on the electron-impact excitation of helium have been well summarized through 1977 in the reviews of Bransden and McDowell [14,15] for intermediate-energy incident electrons. In the experimental arena, the only new DCS's that have been reported since the Bransden-McDowell review are by Brunger *et al.* [16] and those reported here. Westerveld, Heideman, and van Eck [17] determined integral $n\ ^1P$ ($n=2,3$) excitation cross sections from 30 to 2000 eV by normalization to the Born approximation at high incident electron energy and by applying approximate cascade corrections. Shemansky *et al.* [18] reported integral electron-impact excitation cross sections for $n\ ^1P$ ($n=2,3,4$) excitation in the 22 to 2000-eV range that were obtained by normalizing the helium $2\ ^1P$ emission cross section against H Lyman-α emission and the Born approximation at high energy. Cascade corrections were then applied and the two methods gave results that agreed within 3%. Recent theoretical reviews on the subject of electronic excitation

have been provided by Callaway [19], Walters [20], Itikawa [21], and quite recently by Fabrikant *et al.* [22]. A major development from the theoretical side in recent years was the reporting of 5-, 11-, and 19-state R-matrix results [23–25] for electron-impact excitation of helium.

The purpose of this paper is to report first-order many-body theory (FOMBT) results for electron-impact excitation to the helium $n\,^1P$ ($n=2,3,\ldots,6$) levels for incident electron energies from threshold to 500 eV and recently obtained experimental data for excitation of $2\,^1P$, and $3\,^1P$, $3\,^1D$, and $3\,^3D$ unresolved levels at 30, 50, and 60 (at one angle) and 100 eV. FOMBT, which has been used in the past to calculate the electron-impact coherence parameters for excitation of $n\,^1$P levels of helium [7,8,26], and electron-impact excitation DCS's and ICS's for the excitation of the $n\,^1S$, $n\,^3S$, and $n\,^1P$ ($n=2,3$) levels of helium in the 25 eV $\leq E \leq$ 81.6 eV energy range [27,28], were used to obtain the cross-section results reported here. The present FOMBT results extend the energy range in the case of $n\,^1P$ ($n=2,3$) excitation up to 500-eV incident electron energy and results were also obtained for the first time for electron-impact DCS's and ICS's in the case of excitation of the $n\,^1P$ ($n=4,5,6$) levels. The experimental data reported here were obtained by measuring relative scattering intensities and using the helium elastic-scattering cross sections as the standard for normalization of the data to the absolute scale. Extensive comparisons are made between available experimental and theoretical cross sections. The companion paper to this one reports new experimental and theoretical results for the differential and integral cross sections associated with excitation of the individual collision-frame magnetic sublevels ($M=0,\pm1$) for the $n\,^1P$ levels in helium [29(a)]. Results for $n\,^1S$, $n\,^3S$, and $n\,^3P$, obtained from the same electron-energy-loss data will be reported in a future publication [29(b)].

Note. In this paper, we call the collection of magnetic sublevels for a specific n, the $n^{2S+1}L$ "level," and reserve the term "state" for identifying the individual magnetic sublevels.

Notation of $d\sigma/d\Omega$ for the theoretical differential cross section and DCS for the experimentally obtained quantity are used interchangeably here because they are equivalent to within experimental error. DCS is also used for the abbreviation of "differential cross section." Correspondingly, the symbols σ for the theoretical and Q for the experimental integral cross sections are used interchangeably and the abbreviation ICS stands for "integral cross section."

II. EXPERIMENTAL TECHNIQUES AND PROCEDURES

The electron-impact spectrometer and procedures used to obtain the helium data reported here have been described in detail elsewhere [30–33], so only a brief summary will be given here. The spectrometer consists of a double hemispherical gun and detector, both with cylindrical electrostatic optics, and the target beam of atomic helium was formed by a capillary array. Pulse-counting and multichannel scaling techniques were used to generate energy-loss spectra. A typical electron-energy-loss spectrum extending beyond the $n=4$ manifold is shown in Fig. 1. Special care was taken to make the scattered electron detection efficiency independent of the electron residual energy. This was achieved by independently varying the potentials on two of the seven-element detector lens during the electron-energy-loss sweep [34] and by experimentally verifying that the applied voltages were optimum for both the elastic and inelastic electron signal detections by iterative retuning for maximum intensity in these features. The scattering angles (θ) were calibrated based on the symmetry of the $2\,^1P$ scattering signal around nominal zero angle and the electron-impact energy scale was calibrated against the 19.36-eV resonance in the helium elastic channel at 90° scattering angle.

Energy-loss spectra containing the $n=2$ and 3 excitation manifolds were obtained at 30-, 50-, and 100-eV impact energies, and at scattering angles ranging from 5° to 140°. From these spectra, scattering intensities for excitation of the inelastic features associated with the $2\,^3S$, $2\,^1S$, $2\,^3P$, $3\,^3S$, $3\,^1S$, $3\,^3P$, and with the unresolved $3\,^1P$, $3\,^1D$, $3\,^3D$ levels were determined relative to the $2\,^1P$ scattering intensity. These relative scattering intensities were obtained as the integrated count rates under the individual spectral features from which a smooth (and small) background-scattering contribution was subtracted. In a separate experiment, the scattering intensity for excitation of the $2\,^1P$ level, relative to that for elastic scattering, was measured for each impact energy and scattering angle. The relative intensities so obtained were multiplied by the corresponding helium elastic-scattering cross sections measured by Register, Trajmar, and Srivastava [30] to convert them to absolute the $2\,^1P$ DCS's. The relative (with respect to $2\,^1P$) scattering intensities for all inelastic features were then normalized by utilizing the absolute $2\,^1P$ DCS's. We are presenting here only the results for the unresolved ($3\,^1P, 3\,^1D, 3\,^3D$) excitation. Cross sections for other inelastic processes will be published elsewhere [29(b)]. For scattering angles less than 5° at 100 eV and 10° at 30 and 50 eV, the direct beam contribution to the elastic-scattering signal became significant and caused large uncertainties in this normalization procedure. The upper limit in the scattering angle was determined by physical interference of the gun and detector structures.

In estimating the error limits for an inelastic DCS, we considered the statistical errors in the intensity measurements, the errors associated with the determination of scattering intensity ratios, as well as the error limits given by Register, Trajmar, and Srivastava [30] for the elastic DCS. The overall error was obtained as the square root of the sum of the squares of the contributing errors. The DCS's were extrapolated to 0° and to 180° and integrated to obtain the integral excitation cross sections reported here. The extrapolation procedure into the experimentally inaccessible angular regions, which was guided by FOMBT theoretical results, introduces an additional error of 5% to 10% to the ICS values reported here. When combined with the DCS errors, this contribution raises the overall error for the ICS by 1% to 3% above the DCS error for the values reported in Tables I and II.

III. THEORETICAL FOUNDATIONS

First-order many-body theory applied to the description of electron-atom inelastic scattering was first introduced by Csanak, Taylor, and Yaris [37] and many-body theory in this lowest-order form can be considered to be one of many possible forms of a distorted-wave approximation [38]. It is important to emphasize that while there are many different ways to introduce a distortion potential in the DWA, there is only a *single* FOMBT that is consistent with the foundations of many-body theory. This FOMBT incorporates static and exchange distortion effects on the free-electron wave functions in a well-prescribed fashion, and the inelastic scattering T matrix consists of direct and exchange scattering amplitudes. The fundamental formulas of FOMBT, and their application describing excitation of the atomic states of helium, have been reported earlier [26–28], and only a brief summary will be given here.

The inelastic-scattering T matrix for excitation of helium in FOMBT is given by the formula [37,38]

$$T^{\mathrm{FOMBT}}_{\bar{0}\tilde{p},\bar{n}\tilde{q}} = \int dx_1 dx_2 f^{(-)\mathrm{HF}^*}_{\tilde{q}}(x_1) \times f^{(+)\mathrm{HF}}_{\tilde{p}}(x_2) V_{\bar{0}\bar{n}}(x_1 x_2) , \quad (1)$$

where $\tilde{p} \equiv (\mathbf{p}, m_s)$ and $\tilde{q} \equiv (\mathbf{q}, m_s')$ refer to the linear momentum $(\mathbf{p},\mathbf{q})$ and spin (m_s, m_s') coordinates of the incident and scattered electrons; $f^{(+)\mathrm{HF}}_{\tilde{p}}(x)$ and $f^{(-)\mathrm{HF}}_{\tilde{p}}(x)$ are the continuum Hartree-Fock (HF) (or static-exchange) orbitals of helium with outgoing- and incoming-wave boundary conditions, respectively; $\bar{0}$ and $\bar{n}$ refer to the collection numbers of the initial (ground) and final (excited) helium states, respectively; and the symbols x_1, x_2 refer to the combined spatial $(\mathbf{r}_1, \mathbf{r}_2)$ and spin (σ_1, σ_2) coordinates of the electron.

The quantity $V_{\bar{0}\bar{n}}(x_1, x_2)$ is defined by the formula (using Hartree atomic units)

$$V_{\bar{0}\bar{n}}(x_1,x_2) = \delta(x_1 - x_2) \int \frac{dx'}{|\mathbf{r}_1 - \mathbf{r}'|} X^{\mathrm{RPA}}_{\bar{n}}(x',x') - \frac{1}{|\mathbf{r}_1 - \mathbf{r}_2|} X^{\mathrm{RPA}}_{\bar{n}}(x_1,x_2) , \quad (2)$$

where $X^{\mathrm{RPA}}_{\bar{n}}(x_1, x_2)$ is the random-phase approximation (RPA) for the transition density matrix [8,37] between states $\bar{n}$ and $\bar{0}$, $\delta(x_1 - x_2) = \delta(\mathbf{r}_1 - \mathbf{r}_2)\delta_{\sigma_1\sigma_2}$, where $\delta(\mathbf{r}_1 - \mathbf{r}_2)$ is the Dirac delta function and $\delta_{\sigma_1\sigma_2}$ is the Kronecker delta function. The transition density matrix $X_{\bar{n}}(x, x')$ between states $\bar{n}$ and $\bar{0}$, using wave-function terminology, is defined by the formula

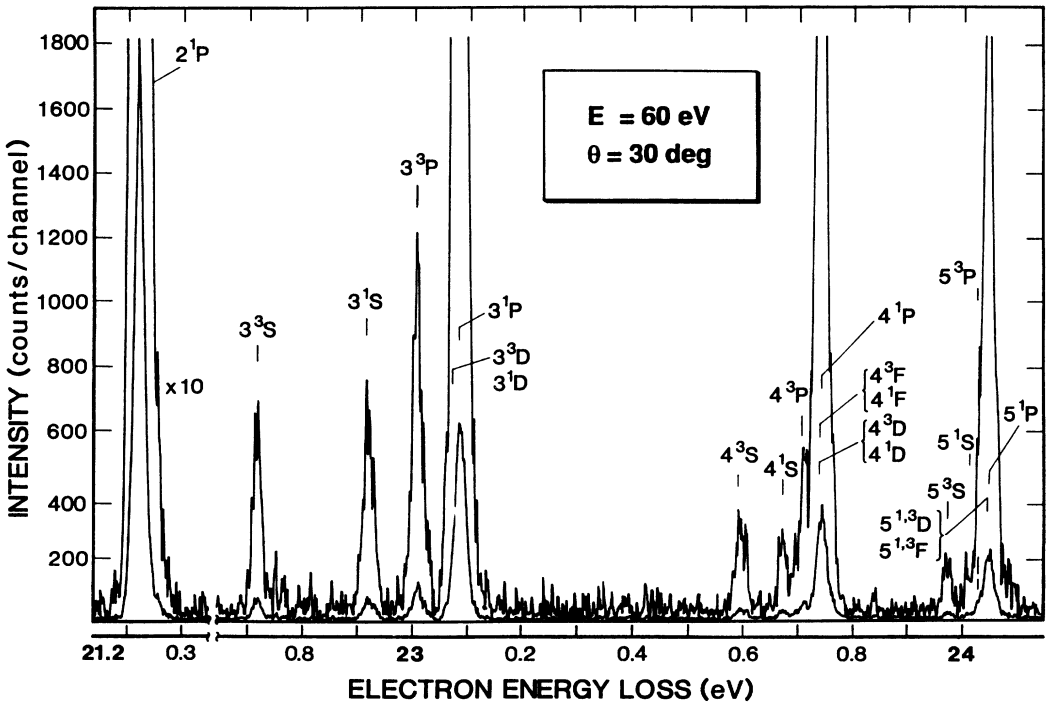

FIG. 1. Electron-impact energy-loss spectrum in helium for $E = 60$ eV incident electron energy and for a scattering angle of 30°. Instrumental resolution is estimated to be about 0.018 eV (FWHM). The energy-loss scale between the $n = 2$ and 3 manifolds has been compressed in the figure.

$$X_{\bar{n}}(x,x')=N\int \varphi^*_{\bar{n}}(x,x_2,\ldots,x_N)\varphi_{\bar{0}}(x',x_2,\ldots,x_N) \times dx_2,\ldots,dx_N\ , \tag{3}$$

where $\varphi_{\bar{0}}(x_1,x_2,\ldots,x_N)$ and $\varphi_{\bar{n}}(x_1,x_2,\ldots,x_N)$ refer to the ground ($\bar{0}$) and excited- ($\bar{n}$) state wave functions of the atomic system, respectively.

It has also been shown [8,26] that, for the $n\,^1P$ ($n=2,3$) excited state of helium, the RPA transition density matrix is well approximated by taking $\varphi_{\bar{0}}$ in the HF approximation and $\varphi_{\bar{n}}$ in the fixed-core HF approximation. This calculational scheme was adopted in the work reported here, and the atomic orbitals were obtained by using the computational techniques and computer programs of Cowan [39]. In this approximation, we obtain for Eq. (3), specifically for a $n\,^1P_{M_L}$ state

$$X^{\mathrm{RPA}}_{n\,^1P_{M_L}}(x,x')=\frac{1}{\sqrt{2}}\phi^*_{npM_L}(\mathbf{r})\phi_{ls}(\mathbf{r}') \times[\alpha^*(\sigma)\alpha(\sigma')+\beta^*(\sigma)\beta(\sigma')]\ , \tag{4}$$

where ϕ_{1s} is the (normalized) ground-state HF orbital and ϕ_{npM_L} is the (normalized) excited-states fixed-core HF orbital of the $n\,^1P_{M_L}$ state of helium.

Inserting Eqs. (3) and (4) into Eq. (2), we obtain

$$V_{\bar{0},n\,^1P_{M_L}}(x_1,x_2)=\delta(x_1-x_2)\sqrt{2}\int\frac{\phi^*_{npM_L}(\mathbf{r}')\phi_{1s}(\mathbf{r}')}{|\mathbf{r}_1-\mathbf{r}'|}d\mathbf{r}' -\frac{1}{|\mathbf{r}_1-\mathbf{r}_2|}\frac{1}{\sqrt{2}}\phi^*_{npM_L}(\mathbf{r}_2)\phi_{1s}(\mathbf{r}_1)[\alpha^*(\sigma_1)\alpha(\sigma_2)+\beta^*(\sigma_1)\beta(\sigma_2)]\ , \tag{5}$$

which, in turn, gives for T matrix [via Eq. (1)],

TABLE I. Experimental DCS (10^{-18} cm^2/sr) and ICS (10^{-18} cm^2) results for excitation of the $2\,^1P$ level of helium.

θ (deg)	30 eV	50 eV	60 eV[a]	80 eV[a]	100 eV
5		28.9	40.0	52.4	78.9
7				36.0	
10	5.05	17.5	23.0	26.0	29.8
15	3.75	10.7	11.0	10.5	10.9
20	2.77	6.42	5.5	4.3	3.86
25				1.9	
30	1.30	2.16	1.3	0.77	0.53
35				0.41	
40	0.46	0.80	0.36	0.23	0.17
50	0.26	0.38	0.19	0.12	0.080
60	0.15	0.27	0.12	0.080	0.055
70	0.12	0.20			0.038
75			0.083	0.051	
80	0.10	0.16	0.066	0.042	0.027
90	0.097	0.12	0.055	0.034	0.016
100	0.091	0.096			0.014
105			0.045	0.023	
110	0.073	0.077			0.012
120	0.075	0.069	0.034	0.019	0.0097
130	0.099	0.062			0.0071
135			0.030	0.017	
140	0.13	0.045			0.0064
Q (10^{-18} cm^2)[b]	4.5	9.6			10.1
Error limits (±%)					
DCS Ratio	18	14			5
DCS elastic	7	6			7.5
DCS inelastic	19	15	17	17	9

[a]Data of Chutjian and Srivastava published earlier [35] which have been renormalized using the more accurate elastic DCS results of Register, Trajmar, and Srivastava [30].
[b]Q: ICS experimental results obtained as described in the text.

$$T^{\mathrm{FOMBT}}_{\bar{0}\bar{p},\, n\,^1P_{M_L}\bar{q}} = \sqrt{2}\int d\mathbf{r}_1 \int d\mathbf{r}_2 f_{\mathbf{q}}^{(-)\mathrm{HF}^*}(\mathbf{r}_1) f_{\mathbf{p}}^{(+)\mathrm{HF}}(\mathbf{r}_1) \frac{\phi^*_{npM_L}(\mathbf{r}_2)\phi_{1s}(\mathbf{r}_2)}{|\mathbf{r}_1-\mathbf{r}_2|}$$
$$-\frac{1}{\sqrt{2}}\int d\mathbf{r}_1 \int d\mathbf{r}_2 f_{\mathbf{q}}^{(-)\mathrm{HF}^*}(\mathbf{r}_1) f_{\mathbf{p}}^{(+)\mathrm{HF}}(\mathbf{r}_2) \frac{1}{|\mathbf{r}_1-\mathbf{r}_2|}\phi^*_{npM_L}(\mathbf{r}_2)\phi_{1s}(\mathbf{r}_1)\,, \tag{6}$$

where we have assumed the spin factorization,

$$f_{\bar{p}}^{(+)\mathrm{HF}}(x) = f_{\mathbf{p}}^{(+)\mathrm{HF}}(\mathbf{r})\eta_{m_s}(\sigma)\,, \tag{7a}$$

$$f_{\bar{q}}^{(-)\mathrm{HF}}(x) = f_{\mathbf{q}}^{(-)\mathrm{HF}}(\mathbf{r})\eta_{m_s}(\sigma)\,, \tag{7b}$$

for the continuum HF orbitals, with $\eta_{m_s}(\sigma)$ denoting the Pauli spin functions. The first term on the right-hand side of Eq. (6) describes the "direct" electron excitation process; the second term is associated with the "exchange" electron excitation process.

If we define $T^D_{M_L}$ (the direct excitation T matrix) and $T^E_{M_L}$ (the exchange excitation T matrix) by the equations

$$T^D_{M_L} = \int d\mathbf{r}_1 \int d\mathbf{r}_2 f_{\mathbf{q}}^{(-)\mathrm{HF}*}(\mathbf{r}_1) f_{\mathbf{p}}^{(+)\mathrm{HF}}(\mathbf{r}_1)\frac{1}{|\mathbf{r}_1-\mathbf{r}_2|} \times \phi^*_{npM_L}(\mathbf{r}_2)\phi_{1s}(\mathbf{r}_2)\,, \tag{8a}$$

$$T^E_{M_L} = \int d\mathbf{r}_1 \int d\mathbf{r}_2 f_{\mathbf{q}}^{(-)\mathrm{HF}^*}(\mathbf{r}_1) f_{\mathbf{p}}^{(+)\mathrm{HF}}(\mathbf{r}_2)\frac{1}{|\mathbf{r}_1-\mathbf{r}_2|} \times \phi^*_{npM_L}(\mathbf{r}_2)\phi_{1s}(\mathbf{r}_1)\,, \tag{8b}$$

TABLE II. Columns 2–6 are the sum of the experimental DCS's (10^{-20} cm^2/sr) and ICS's (10^{-20} cm^2) for excitation of the unresolved $3\,^1P$, $3\,^1D$, $3\,^3D$ levels of helium. The last two columns are estimates of the DCS's (10^{-20} cm^2/sr) for the excitation of the $3\,^1P$ level.

	$3\,^1P+3\,^1D+3\,^3D$					$3\,^1P$	
θ (deg)	30 eV	29.2 eV[a]	39.7 eV[a]	50 eV	100 eV	80 eV[b]	100 eV[b]
5		87	370	569	1800	1190	1920
7						880	1470
10	91	70	280	360	754	580	830
15	66		180	244	306	270	340
20	54	35	110	157	119	110	130
25			68			46	41
30	30	21	37	61	17	21	15
35		20					
40	12	11		23	5.3	7.3	5.2
45		7.0	8				
50	7.3	4.8		10	2.5	4.7	
55		4.2					
60	5	3.3	4	7.7	1.6	3.1	1.9
65		2.1					
70	3.4			5.9	1.2		
75		2.2	2.6				
80	3.2			4.7	0.96		
90	3.1	2	1.9	3.8	0.50	1.3	0.63
100	2.9	2.2		3.2	0.46		
105		2	2				
110	2.4	2	1.8	2.3	0.34	0.71	0.41
120	2.5	2.2	1.6	2.1	0.29		
130	3.6	2.4		1.7	0.23		
135		2.4	1.9			0.62	0.37
140	4.1			1.6	0.19		
Q (10^{-20} cm^2)	1.05				2.34	2.6	
Error limits (±%)							
Ratio	21	14		14	8		
DCS elastic	7	6		6	7.5		
DCS inelastic	22	22		25		20	20

[a]Results of Chutjian and Thomas [28]. (Renormalization was not feasible.)

[b]$3\,^1P$ results were calculated from the $(3\,^1P)$/elastic intensity ratios of Chutjian [36] and from the elastic DCS data of Register, Trajmar, and Srivastava [30].

then Eq. (6) can be rewritten as

$$T_{\bar{0}\bar{p}\,n\,^1P_{M_L}\bar{q}|} = \sqrt{2}\left(T^D_{M_L} - \tfrac{1}{2}T^E_{M_L}\right)\delta_{m_s m_s'} . \tag{9}$$

This separation is useful computationally because different numerical techniques are required for the two terms. In calculating $T^D_{M_L}$ and $T^E_{M_L}$, it is convenient to expand both $f_{\mathrm{p}}^{(+)\mathrm{HF}}(\mathbf{r})$ and $f_{\mathrm{q}}^{(-)\mathrm{HF}}(\mathbf{r})$ in terms of partial waves according to

TABLE III. Comparison of experimental and calculated DCS results (10^{-20} cm^2/sr) at $E=60$ eV incident electron energy and $\theta=30°$ scattering angle (from Fig. 1).

Level(s)	Expt.	FOMBT
$2\,^1P$	125	168.7
$3\,^1P+3\,^1D,3\,^3D$	42	51.8
$4\,^1P+4\,^1D,4\,^3D+4\,^3F$	24	21.9[a]
$5\,^1P+5\,^1D,5\,^3D+5\,^3F$	15	11.2[a]

[a]The $n\,^1F,n\,^3F$ contributions are considered negligible and were not included in this calculation.

TABLE IV. DCS results (10^{-19} cm^2/sr) for the excitation of the $2\,^1P$ level helium obtained from FOMBT calculations.

θ (deg)	30 eV	50 eV	81 eV	100 eV	500 eV
0	52.8	383.0	1070.0	1492.0	10780.0
1	52.7	381.0	1053.0	1455.0	6425.0
2	52.4	375.0	1004.0	1355.0	2794.0
4	51.4	351.0	842.0	1051.0	716.0
6	49.7	315.0	652.0	743.0	240.0
8	47.5	274.0	481.0	504.0	88.8
10	44.8	231.0	346.0	337.0	34.1
12	41.8	192.0	245.0	224.0	13.3
14	38.5	156.0	173.0	149.0	5.29
16	35.1	125.0	121.0	98.9	2.13
20	28.3	77.4	58.4	43.5	0.384
25	20.6	40.8	23.3	15.51	0.0779
35	9.54	10.56	3.93	2.28	0.0274
40	6.17	5.42	1.90	1.32	0.0206
45	3.90	2.99	1.141	0.740	0.0157
50	2.46	1.87	0.852	0.588	0.0121
55	1.58	1.37	0.721	0.509	0.009 43
60	1.08	1.15	0.640	0.451	0.007 61
65	0.804	1.03	0.575	0.399	0.006 30
70	0.665	0.959	0.517	0.353	0.005 33
75	0.600	0.900	0.465	0.311	0.004 61
80	0.572	0.846	0.419	0.277	0.004 01
85	0.561	0.794	0.378	0.246	0.003 55
90	0.555	0.747	0.344	0.221	0.003 18
95	0.549	0.705	0.316	0.202	0.002 88
100	0.542	0.668	0.293	0.187	0.002 64
105	0.533	0.639	0.275	0.175	0.002 41
110	0.523	0.616	0.261	0.165	0.002 21
115	0.513	0.599	0.250	0.158	0.002 07
120	0.503	0.587	0.241	0.152	0.001 96
125	0.494	0.580	0.235	0.147	0.001 87
130	0.486	0.576	0.231	0.144	0.001 76
135	0.479	0.575	0.228	0.142	0.001 65
140	0.473	0.576	0.227	0.140	0.001 60
145	0.469	0.579	0.226	0.139	0.001 57
150	0.466	0.582	0.226	0.139	0.001 53
155	0.464	0.586	0.226	0.138	0.001 49
160	0.463	0.589	0.226	0.138	0.001 45
165	0.462	0.592	0.227	0.138	0.001 44
170	0.461	0.594	0.227	0.137	0.001 43
175	0.461	0.596	0.227	0.137	0.001 42
180	0.461	0.596	0.227	0.137	0.001 42

TABLE V. FOMBT differential (10^{-19} cm^2/sr) and integral cross sections (10^{-19} cm^2) for excitation of the $3\,^1P$, $3\,^1D$, $3\,^1D$ levels in helium. Columns 5 and 9, denoted by the label $\mathcal{S}$, are the sum of the previous three columns and numbers in square brackets denote the powers of 10 times the entry.

θ (deg)	$3\,^1P$	$3\,^1D$	$3\,^3D$	$\mathcal{S}$	$3\,^1P$	$3\,^1D$	$3\,^3D$	$\mathcal{S}$
		30 eV				40 eV		
0	7.16	0.158	0.456	7.77	34.8	0.750	0.417	35.9
5	6.94	0.155	0.453	7.55	32.5	0.727	0.414	33.6
10	6.31	0.146	0.443	6.90	26.8	0.660	0.404	27.9
15	5.40	0.131	0.428	5.96	19.9	0.556	0.388	20.8
20	4.38	0.113	0.406	4.90	13.6	0.432	0.366	14.4
25	3.37	0.923[−1]	0.379	3.84	8.75	0.311	0.337	9.40
30	2.49	0.726[−1]	0.349	2.91	5.36	0.208	0.303	5.87
35	1.76	0.550[−1]	0.315	2.13	3.17	0.132	0.266	3.57
40	1.20	0.406[−1]	0.280	1.52	1.83	0.808[−1]	0.227	2.14
45	0.801	0.298[−1]	0.246	1.08	1.06	0.493[−1]	0.190	1.30
50	0.525	0.223[−1]	0.212	0.759	0.634	0.313[−1]	0.155	0.820
55	0.344	0.175[−1]	0.181	0.543	0.414	0.218[−1]	0.124	0.560
60	0.231	0.147[−1]	0.154	0.400	0.307	0.171[−1]	0.985[−1]	0.423
65	0.165	0.134[−1]	0.132	0.310	0.258	0.147[−1]	0.778[−1]	0.351
70	0.128	0.131[−1]	0.114	0.255	0.236	0.135[−1]	0.619[−1]	0.311
75	0.109	0.133[−1]	0.101	0.223	0.226	0.128[−1]	0.504[−1]	0.289
80	0.996[−1]	0.139[−1]	0.427[−1]	0.156	0.220	0.123[−1]	0.923[−1]	0.325
85	0.957[−1]	0.148[−1]	0.381[−1]	0.149	0.214	0.118[−1]	0.882[−1]	0.314
90	0.939[−1]	0.159[−1]	0.360[−1]	0.146	0.208	0.114[−1]	0.881[−1]	0.308
100	0.917[−1]	0.184[−1]	0.370[−1]	0.147	0.195	0.109[−1]	0.971[−1]	0.303
110	0.886[−1]	0.215[−1]	0.420[−1]	0.152	0.183	0.109[−1]	0.115	0.309
120	0.848[−1]	0.249[−1]	0.482[−1]	0.158	0.174	0.114[−1]	0.136	0.321
130	0.814[−1]	0.285[−1]	0.542[−1]	0.164	0.169	0.122[−1]	0.159	0.340
140	0.790[−1]	0.320[−1]	0.592[−1]	0.170	0.166	0.130[−1]	0.179	0.358
150	0.777[−1]	0.350[−1]	0.628[−1]	0.176	0.166	0.139[−1]	0.196	0.376
160	0.771[−1]	0.374[−1]	0.652[−1]	0.180	0.167	0.146[−1]	0.209	0.391
170	0.770[−1]	0.389[−1]	0.666[−1]	0.183	0.168	0.151[−1]	0.217	0.440
180	0.770[−1]	0.394[−1]	0.670[−1]	0.183	0.168	0.152[−1]	0.219	0.402
Integral cross section	6.65	0.379	2.11	9.14	17.6	0.625	1.21	19.4
		50 eV				100 eV		
0	73.5	1.45	0.243	75.0	308.0	3.57	0.238[−1]	311.0
5	65.6	1.39	0.241	67.2	199.0	3.18	0.244[−1]	202.0
10	48.4	1.21	0.236	49.8	84.0	2.22	0.259[−1]	86.2
15	31.3	0.947	0.227	32.5	33.0	1.23	0.268[−1]	34.3
20	18.6	0.665	0.213	19.5	12.7	0.573	0.253[−1]	13.3
25	10.4	0.424	0.194	11.0	4.80	0.234	0.212[−1]	5.06
30	5.64	0.249	0.171	6.06	1.82	0.879[−1]	0.160[−1]	1.92
35	2.98	0.138	0.145	3.26	0.736	0.324[−1]	0.111[−1]	0.780
40	1.57	0.738[−1]	0.119	1.76	0.354	0.130[−1]	0.725[−2]	0.374
45	0.868	0.402[−1]	0.947[−1]	1.00	0.220	0.661[−2]	0.457[−2]	0.231
50	0.530	0.237[−1]	0.733[−1]	0.627	0.170	0.453[−2]	0.281[−2]	0.177
55	0.375	0.162[−1]	0.555[−1]	0.447	0.146	0.375[−2]	0.172[−2]	0.152
60	0.305	0.128[−1]	0.415[−1]	0.359	0.129	0.332[−2]	0.106[−2]	0.133
65	0.272	0.112[−1]	0.310[−1]	0.314	0.114	0.297[−2]	0.681[−3]	0.118
70	0.254	0.103[−2]	0.234[−1]	0.288	0.101	0.264[−2]	0.468[−3]	0.104
75	0.239	0.963[−2]	0.183[−1]	0.267	0.897[−1]	0.233[−2]	0.354[−3]	0.928[−1]
80	0.227	0.898[−2]	0.150[−1]	0.251	0.795[−1]	0.205[−2]	0.297[−3]	0.819[−1]
85	0.214	0.837[−2]	0.131[−1]	0.235	0.709[−1]	0.180[−2]	0.273[−3]	0.730[−1]
90	0.202	0.780[−2]	0.122[−1]	0.222	0.639[−1]	0.158[−2]	0.265[−3]	0.658[−1]
100	0.181	0.688[−2]	0.124[−1]	0.200	0.537[−1]	0.124[−2]	0.265[−3]	0.553[−1]
110	0.166	0.630[−2]	0.138[−1]	0.186	0.472[−1]	0.100[−2]	0.263[−3]	0.485[−1]
120	0.157	0.603[−2]	0.153[−1]	0.178	0.432[−1]	0.842[−2]	0.251[−3]	0.460[−1]
130	0.153	0.600[−2]	0.165[−1]	0.176	0.409[−1]	0.739[−2]	0.228[−3]	0.419[−1]
140	0.153	0.610[−2]	0.174[−1]	0.177	0.398[−1]	0.680[−2]	0.200[−3]	0.407[−1]

TABLE V. (*Continued.*)

θ (deg)	$3\,^1P$	$3\,^1D$	$3\,^3D$	$\mathcal{S}$	$3\,^1P$	$3\,^1D$	$3\,^3D$	$\mathcal{S}$
150	0.154	0.626[−2]	0.178[−1]	0.178	0.395[−1]	0.647[−2]	0.173[−3]	0.402[−1]
160	0.156	0.640[−2]	0.178[−1]	0.180	0.393[−1]	0.626[−2]	0.151[−3]	0.401[−1]
170	0.157	0.650[−2]	0.180[−1]	0.182	0.391[−1]	0.615[−2]	0.135[−3]	0.399[−1]
180	0.158	0.653[−2]	0.180[−1]	0.183	0.391[−1]	0.610[−2]	0.131[−3]	0.398[−1]
Integral cross section	24.6	0.790	0.550	25.9	28.7	0.774	0.344[−1]	29.5

$$f_{\mathbf{p}}^{(+)\mathrm{HF}}(\mathbf{r})=\sum_{l_p=0}^{\infty} i^{l_p}\cos[\delta_{l_p}^{\mathrm{HF}}(p)]e^{i\delta_{l_p}^{\mathrm{HF}}(p)}R_{p,l_p}(r)P_{l_p}(\cos\theta) \tag{10a}$$

and

$$f_{\mathbf{q}}^{(-)\mathrm{HF}}(\mathbf{r})=\frac{4\pi}{qr}\sum_{l_q=0}^{\infty}\sum_{m_q=-l_q}^{l_q} i^{l_q}\cos[\delta_{l_q}^{\mathrm{HF}}(q)]e^{i\delta_{l_q}^{\mathrm{HF}}(q)} \times R_{q,l_q}(r)Y_{l_q m_q}^{*}(\hat{q})Y_{l_q m_q}(\hat{r})\,. \tag{10b}$$

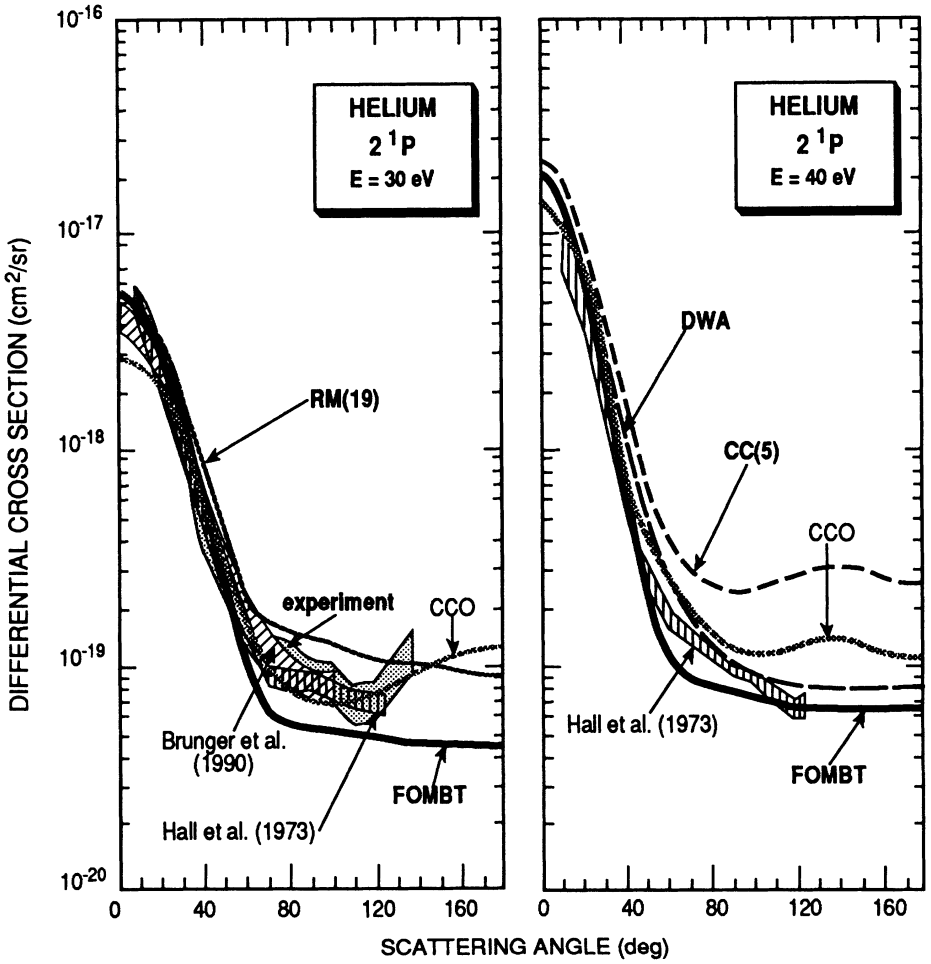

FIG. 2. Comparison of experimental and theoretical DCS's for excitation of the $2\,^1P$ level of helium, at 30 eV (left panel) and 40 eV (right panel) incident electron energies. Theoretical results shown in one or both panels include: the five-state close-coupling calculation results [CC(5)] of Bhadra, Callaway, and Henry [46], the 19-state R -matrix calculation results of Fon, Berrington, and Kingston [25] [RM(19)], results from the distorted-wave approximation (DWA) calculation of Madison and co-workers [41,43] ten-state coupled channels optical calculation (CCO) results of Brunger *et al.* [16], and the present FOMBT results. Experimental results shown are those of Hall *et al.* [47], Brunger *et al.* [16], and from the present study (experiment).

We have chosen the incident electron direction as the positive z axis; θ is the polar angle of $\mathbf{r}$, and $\hat{\mathbf{r}}$ and $\hat{\mathbf{q}}$ refer to the angular coordinates of $\mathbf{r}$ and $\mathbf{q}$, respectively. Without loss of generality, the scattered electron can be assumed to propagate in the (X,Z) plane so that the azimuthal angle of the scattered electron, $\phi_q=0$. (This coordinate system is frequently referred to as the "collision frame.") The functions $R_{p,l_p}(r)$ and $R_{q,l_q}(r)$ are the appropriate radial continuum *HF* orbitals with associated phase shifts $\delta_{l_p}^{\mathrm{HF}}(p)$ and $\delta_{l_q}^{\mathrm{HF}}(q)$, respectively, $P_l(z)$ refers to the usual Legendre polynomial, and $Y_{lm}(\hat{\mathbf{r}})$ is the customary spherical harmonic [40].

Inserting Eqs. (10a) and (10b) into (8a) and (8b), and writing the target orbitals in the form

$$\phi_{1s}(\mathbf{r})=\frac{R_{ls}(r)}{r}Y_{00}(\hat{\mathbf{r}}) \tag{11a}$$

$$\phi_{npM_L}(\mathbf{r})=\frac{R_{np}(r)}{r}Y_{1M_L}(\hat{\mathbf{r}})\ ,\quad \mathrm{M_L}=0,\pm1 \tag{11b}$$

where M_L refers to the magnetic sublevel on the $n\ ^1P$ level, we obtain

$$T_{M_L}^{D}=-\frac{4\pi}{pq}i\sum_{l_p,l_q}(-1)^{(1/2)(l_p-l_q+1)}e^{i\Delta(p,l_p;q,l_q)}\frac{(2l_q+1)}{\sqrt{3}}C_{-M_L M_L 0}^{l_q 1 l_p}C_{000}^{l_q 1 l_p}\left[\frac{(l_q-M_L)!}{(l_q-M_L)!}\right]^{1/2}T_{p,l_p,q,l_q}^{D}P_{i_q}^{M_L}(\cos\theta_q) \tag{12a}$$

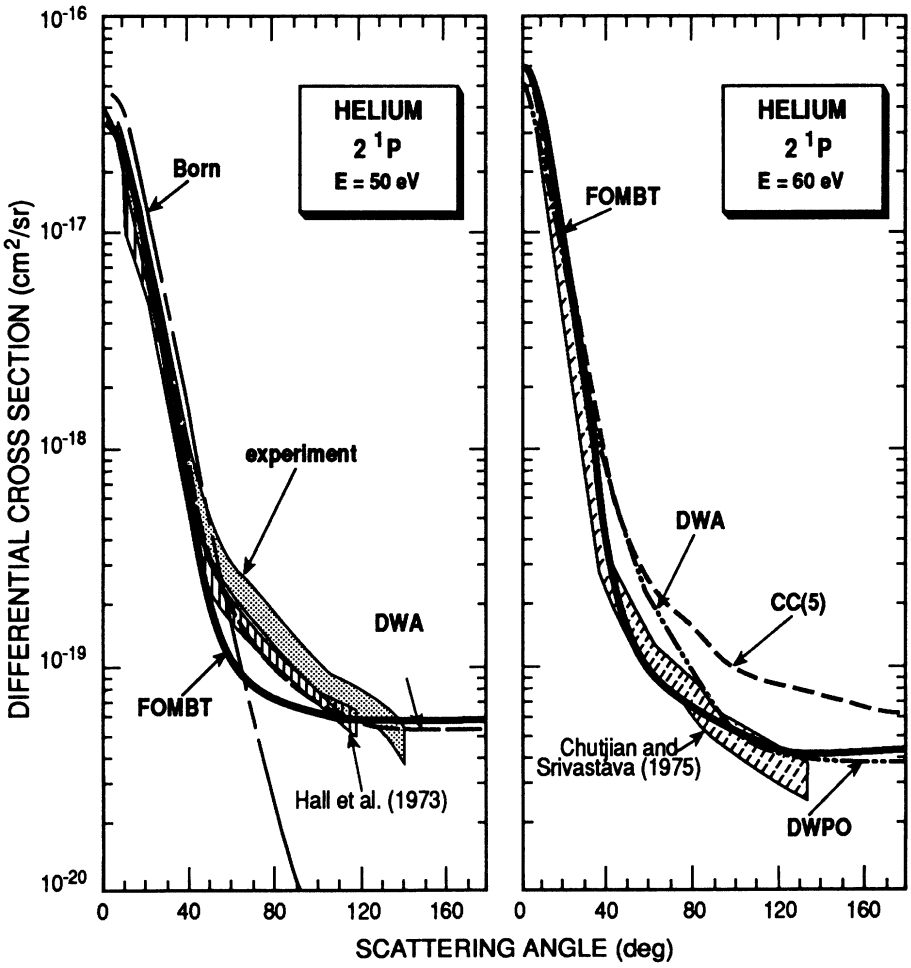

FIG. 3. Same as Fig. 2, except for 50-eV (left panel) and 60-eV (right panel) incident electron energies. Theoretical results shown are as follows: present FOMBT results, five-state close-coupling results of Bhadra, Callaway, and Henry [46] [CC(5)], the distorted-wave polarized orbital (DWPO) results of Scott and McDowell [48], and DWA results of Madison and co-workers [41,43]. The curve labeled Born denotes first-order Born-approximation results from the present study. The shaded areas represent experimental results (with their error limits) of Hall *et al.* [47], Chutjian and Srivastava [35] (renormalized), as well as the present measurements labeled "experiment."

and

$$T^E_{M_L}=-\frac{4\pi}{pq}i\sum_{l_p,l_q}(-1)^{(1/2)(l_p-l_q+1)}e^{i\Delta(p,l_p;q,l_q)}\sqrt{3}C^{l_q1l_p}_{-M_LM_L0}C^{l_q1l_p}_{000}\left[\frac{(l_q-M_L)!}{(l_q+M_L)!}\right]^{1/2}T^E_{p,l_p,q,l_q}P^{M_L}_{l_q}(\cos\theta_q)\ , \tag{12b}$$

where

$$\Delta(p,l_p,q,l_q)\equiv\delta_{l_p}(p)+\delta_{l_q}(q)\ . \tag{13}$$

We have also introduced the following definitions for the direct and exchange radial integrals

$$T^D_{p,l_p,q,l_q}=\int_0^\infty\int_0^\infty R_{p,l_p}(r_1)R_{q,l_q}(r_1)v_1(r_1,r_2)\times R_{1s}(r_2)R_{np}(r_2)dr_1dr_2 \tag{14a}$$

and

$$T^E_{p,l_p,q,l_q}=\int_0^\infty\int_0^\infty R_{p,l_p}(r_1)R_{np}(r_1)v_{l_q}(r_1,r_2)\times R_{1s}(r_2)R_{q,l_q}(r_2)dr_1dr_2\ , \tag{14b}$$

where $v_\lambda(r_1,r_2)$ is the λth term [40] in the multipole expansion of the $(1/|\mathbf{r}_1-\mathbf{r}_2|)$ Coulomb interaction potential.

If we also introduce definitions for the direct and exchange radial "transition potentials,"

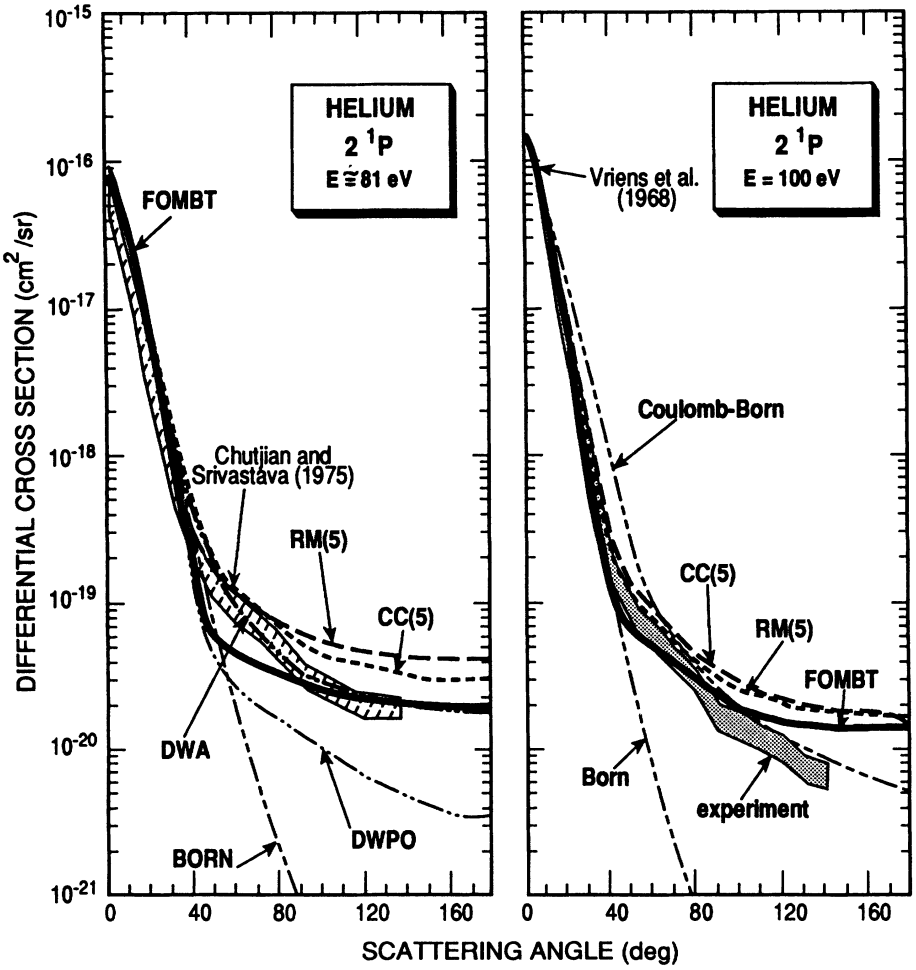

FIG. 4. Same as Fig. 2, except for $E\cong 81$ eV (left panel) and $E=100$ eV (right panel) incident electron energies. Theoretical results, shown are as follows: present FOMBT results, five-state R-matrix results of Fon, Berrington, and Kingston [25] [RM(5)], five-state close-coupling results of Bhadra, Callaway, and Henry [46] [CC(45)], DWA results of Madison and co-workers [41,43], and DWPO results of Scott and McDowell [48]. The results of the present first-order Born approximation and those of the Coulomb-Born approximation of Hidalgo and Geltman [49] are also shown. The experimental results shown are from Chutjian and Srivastava [35] at 80 eV (renormalized), Vriens, Simpson, and Mielczarek [50], and present study at 100 eV, labeled "experiment".

$$V^{\lambda}_{1s,np}(r)=\int_0^{\infty} R_{1s}(r_2)R_{np}(r_2)v_{\lambda}(r,r_2)dr_2 \ , \tag{15a}$$

$$V^{\lambda}_{1s,ql_q}(r)=\int_0^{\infty} R_{1s}(r_2)R_{q,l_q}(r_2)v_{\lambda}(r,r_2)dr_2 \ , \tag{15b}$$

then we can write the radial integrals in the compact form

$$T^{D}_{p,l_p,q,l_q}=\int_0^{\infty} R_{p,l_p}(r)R_{q,l_p}(r)V^{1}_{1s,np}(r)dr \tag{16a}$$

and

$$T^{E}_{p,l_p,q,l_q}=\int_0^{\infty} R_{p,1_p}(r)R_{np}(r)V^{1}_{1s,ql_q}(r)dr \ . \tag{16b}$$

In order to greatly accelerate the numerical convergence of the partial-wave expansion for the direct T-matrix elements [Eq. (12a)], the partial-wave Born approximation T-matrix elements are subtracted, term by term, inside the summation, and then the closed-form (all l values) Born amplitude is added back outside the summation [5,8,26]. The advantage of this procedure is that undistorted partial waves are included to infinite order in closed form which results in very rapid convergence of the sum over partial waves. A "tail correction" was also incorporated into the calculations of the radial integrals [13] to ensure that the very long range (r^{-2}) dipolelike interactions were calculated accurately.

The magnetic-sublevel ($M=0,\pm1$) differential cross sections [27], which are the subject of the following paper, are identified here as

$$\left[\frac{d\sigma}{d\Omega}\right]_{M_L}=\frac{q}{4\pi^2 p}\frac{1}{2}|2T^{D}_{M_L}-T^{E}_{M_L}|^2 \ , \tag{17}$$

and the total (summed over magnetic sublevels) level differential cross section is obtained from

$$\frac{d\sigma}{d\Omega}=\sum_{M_L=-L}^{L}\left[\frac{d\sigma}{d\Omega}\right]_{M_L}=\left[\frac{d\sigma}{d\Omega}\right]_{M_L=0}+2\left[\frac{d\sigma}{d\Omega}\right]_{M_L=1} \tag{18}$$

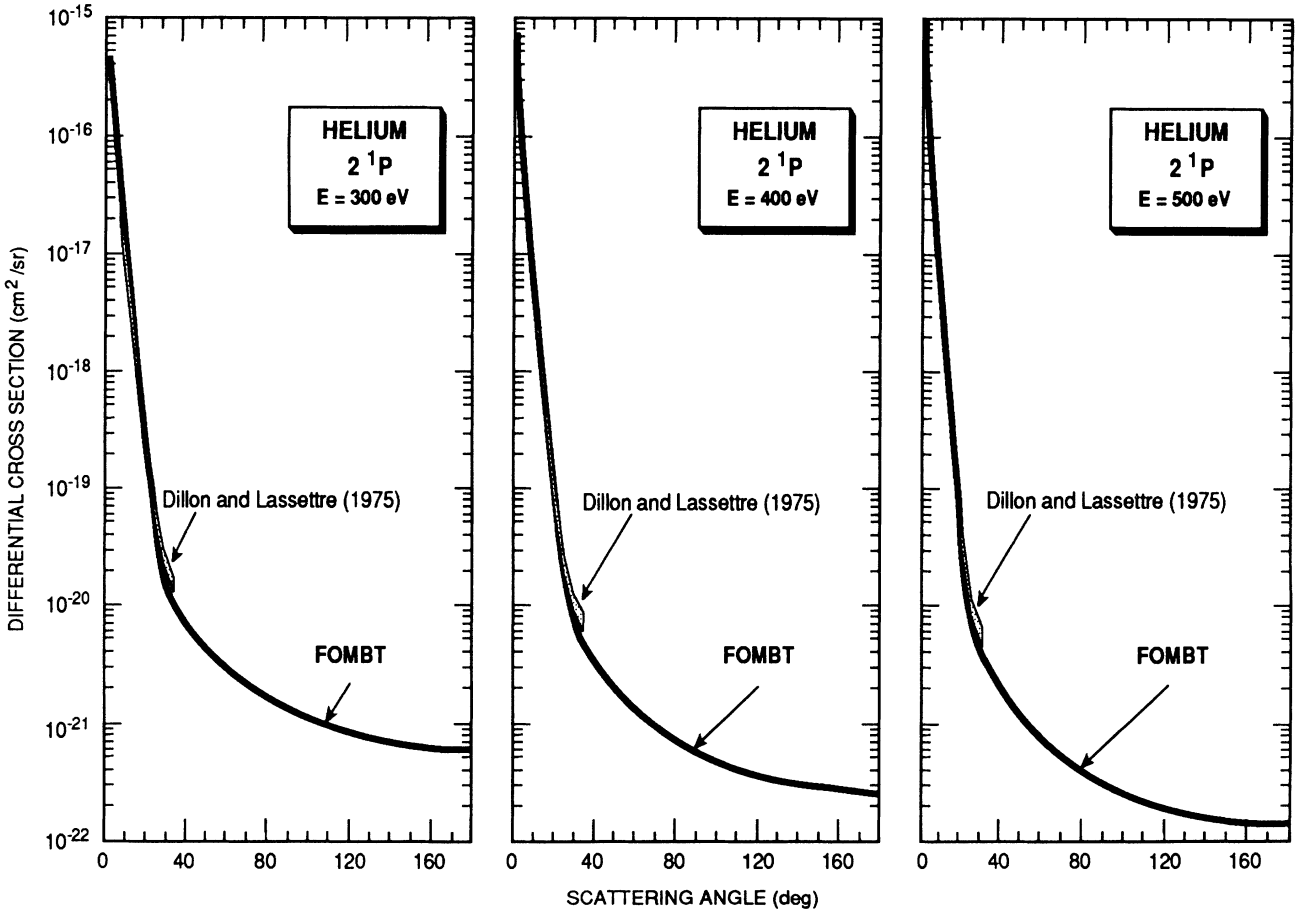

FIG. 5. Same as Fig. 2, except for $E=300$ eV (left panel), $E=400$ eV (middle panel), and $E=500$ eV (right panel) incident electron energies. In this figure the present FOMBT results (solid line) are compared to the experimental results of Dillon and Lassettre [51].

The integral cross section for the excitation on the $n\,^1P$ level is obtained through integration over the whole angular range

$$\sigma(n\,^1P)=\int \frac{d\sigma}{d\Omega}d\Omega \ . \tag{19}$$

The numerical accuracy of the computational codes developed in this research was verified by comparing results from them with both the earlier FOMBT results of Thomas *et al.* [27] and the DWA results of Madison and co-workers [41–43]. The agreement is generally excellent, and any small differences from the earlier FOMBT results can be attributed to small differences in the bound-state target orbitals.

IV. RESULTS AND DISCUSSION

FOMBT results for the DCS's and ICS's for excitation of the $n\,^1P$ ($n=2,3,\ldots,6$) levels in helium for incident electron energies from threshold to 500 eV and experiment data for excitation of the $2\,^1P$ level at 30, 50, and 100 eV are reported here. We also report experimental data corresponding to the sum of the excitation cross sections of the unresolved $3\,^1P, 3\,^1D, 3\,^3D$ levels at these energies because these levels could not be resolved in our experiments.

A. Results

Table I summarizes the new experimental DCS results reported here for incident electron energies of 30, 50, and 100 eV for excitation of the $2\,^1P$ level of helium. Included in Table I are the results of Chutjian and Srivastava [35] at 60- and 80-eV incident electron energies, which have been renormalized to the recent absolute elastic-scattering DCS results of Register, Trajmar, and Srivastava [30] in order to have consistent data at these five incident electron energies.

Columns 2, 5, and 6 in Table II contain the *sum* of the DCS's for excitation of the unresolved $3\,^1P$, $3\,^1D$, $3\,^3D$ levels as measured in this study at incident electron energies of 30, 50, and 100 eV. The data of Chutjian and Thomas [28] for 29.2- and 39.7-eV incident electron energies are given in columns 3 and 4. Columns 7 and 8 in Table II are the DCS results for excitation of the $3\,^1P$ level calculated from the $3\,^1P$ to elastic intensity ratios of Chutjian [36] at 80- and 100-eV incident electron energies, using the absolute elastic-scattering DCS data of Register, Trajmar, and Srivastava [30]. In spite of a claim by Mansky and Flannery [44] to the contrary, *neither Chutjian [36] nor any one else has yet resolved the* $3\,^1P$ *level from the close-lying* $3\,^1D$ *and* $3\,^3D$ *levels in electron-energy-loss spectra.* Chutjian *estimated* the DCS for $3\,^1P$ excitation at 80- and 100-eV incident electron energy by assuming that the $3\,^1D$ and $3\,^3D$ excitation DCS's were

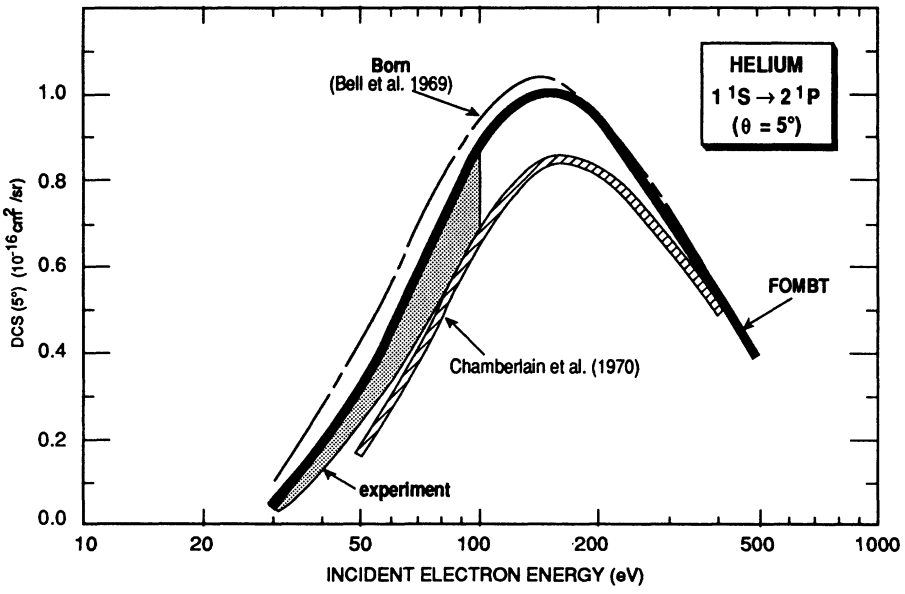

FIG. 6. Comparison of experimental and theoretical results for the dependence of the DCS ($\theta=5°$) on the incident electron energy, for excitation of the $2\,^1P$ level in helium. The solid line denotes the FOMBT results, the dashed line is the first-order Born-approximation results of Bell, Kennedy, and Kingston [52]. The lightly shaded region denotes the present experimental results, and the earlier experimental results of Chamberlain, Mielczarek, and Kuyatt [53] are shown with cross hatching.

TABLE VI. Summary and comparison of $n\,^1P$ ($n=2,3,4,5,6$) integral cross sections (10^{-18} cm^2).

	$2\,^1P$				$3\,^1P$				$4\,^1P$		$5\,^1P$	$6\,^1P$
	Ref. [17][a]	Ref. [18][a]	Present		Ref. [17][a]	Ref. [18][a]	Present[b]		Ref. [18][a]	Present	Present	Present
E (eV)	Expt.	Expt.	Expt.	FOMBT	Expt.	Expt.	Expt.	FOMBT	Expt.	FOMBT	FOMBT	FOMBT
22		0.108										
23		0.379										
24		0.744							0.0416			
25		1.165		1.43				0.144	0.0692	0.0381	0.0152	0.007 58
27.5				2.69				0.375		0.116	0.0516	0.0203
30	3.75	3.408	4.5	4.01	0.74	0.582	1.05	0.665	0.303	0.223	0.102	0.0555
35											0.218	0.121
40	6.43	6.659		8.19	1.38	1.400		1.76	0.614	0.657	0.320	0.180
50	9.52	8.37	9.6	10.39	1.84	2.166	2.34	2.46	0.801	0.928	0.457	0.259
60		9.24		11.44	2.16	2.097		2.73	0.916	1.07	0.528	0.300
70	9.77	9.66		11.84	2.34	2.216		2.87	0.985	1.13	0.562	0.320
80	10.15	9.81			2.43	2.265			1.025		0.575	0.328
81.6				11.87				2.92		1.16	0.568	0.324
90	10.15	9.82			2.45	2.274			1.042		0.507	0.290
100	10.10	9.74	10.1	11.56	2.44	2.258	2.6	2.87	1.046	1.14	0.446	0.255
150	9.18	8.78		10.14	2.26	2.041		2.54	0.967	1.02	0.357	0.204
200	8.30	7.747		8.86	2.08	1.805		2.23	0.860	0.892	0.299	0.171
500	5.07	4.579		5.09	1.29	1.086		1.29	0.500	0.515	0.258	0.147
1000	3.14	2.903			0.79	0.691			0.304			
2000	1.85	1.747			0.47	0.417			0.181			

[a]Corrected for cascade.
[b]($3\,^1P, 3\,^1D, 3\,^3D$) combined.
[c]Calculated at 81.6 eV.

small at these incident energies and by subtracting theoretical DCS's for excitation of the $3\,^1D$ and $3\,^3D$ levels from the peak height in the electron-energy-loss spectra associated with excitation of the combined $3\,^1P$, $3\,^1D$, $3\,^3D$ levels. It is notable that this procedure yields only an estimate of the $3\,^1P$ DCS and does not give experimental data of the DCS's for excitation of the $3\,^1D$ and $3\,^3D$ levels. The only relative DCS data that exists for any of these levels individually are those obtained for the $3\,^3D$ level excitation at 39.7 eV in the 30° to 90° angular range by Chutjian *et al.* [45] using electron-photon coincidence technique. In this paper we have chosen to compare directly the measured DCS for the composite $(3\,^1P, 3\,^1D, 3\,^3D)$ feature with the corresponding quantity obtained from our FOMBT calculations.

Table III contains a summary of the differential-cross-section information deduced from the electron-impact spectrum at 60-eV incident electron energy and $\theta = 30°$ scattering angle (shown in Fig. 1) and a comparison with the corresponding results from FOMBT.

The DCS results obtained from our FOMBT calculations for excitation of the $2\,^1P$ level are given in Table IV and those for the $3\,^1P$, $3\,^1D$, and $3\,^3D$ levels are given in Table V. The FOMBT integral cross-section results for excitation of the $n\,^1P$ ($n = 2,3,4$) levels are given in Table VI along with our experimental results and selected previously reported data. FOMBT results for the integrated cross sections for the $5\,^1P$ and $6\,^1P$ levels are also given in Table VI.

B. Comparison of $2\,^1P$ DCS results

The DCS results obtained from the FOMBT for excitation of the $2\,^1P$ level are compared with selected sets of experimental and theoretical results in Figs. 2–6. These figures show that FOMBT gives quantitative agreement with the experimental data for incident electron energies from 30 to 100 eV and scattering angles $5° \leq \theta \leq 40°$ and for $E > 100$ eV over the entire angular range. These

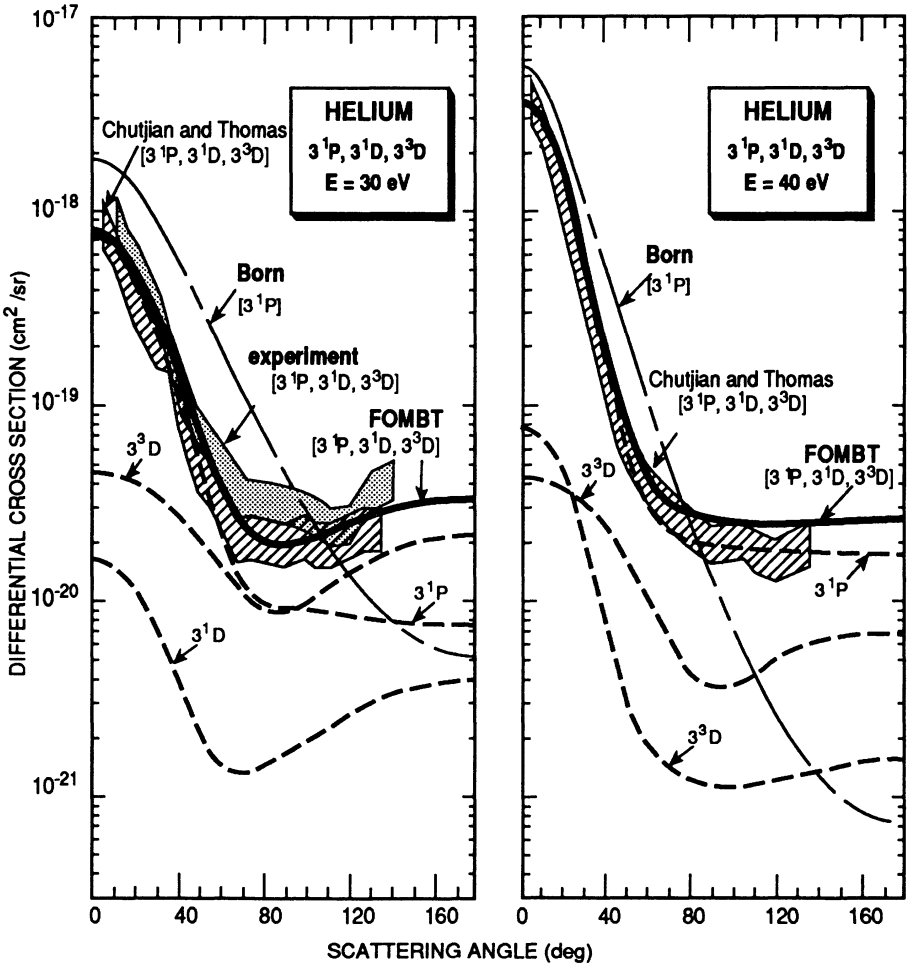

FIG. 7. Comparison of experimental and theoretical DCS's for excitation of the unresolved $3\,^1P, 3\,^1D, 3\,^3D$ levels of helium, at $E \cong 30$ eV (left panel) and $E = 40$ eV (right panel) incident electron energies. The solid line denotes the present FOMBT results for the sum of the three DCS's. The individual DCS's are shown by the appropriately labeled heavy dashed lines. The present first-order Born-approximation results for excitation of the $3\,^1P$ level are also shown. The shaded regions represent the present experimental results (left panel), and those of Chutjian and Thomas [28] (both panels).

figures show that the five-state R-matrix theory results [23] and five-state close-coupling calculation results [46] for the DCS's are too high and their deviation from the experiment data also decreases with increasing energy. Figure 6 shows the FOMBT agrees reasonably well with experimental at $\theta=5°$ scattering angle in the 30 eV $\leq E \leq$ 100 eV electron-energy range. The present experimental DCS values at $\theta=5°$ scattering angle deviate significantly from those obtained by Chamberlain, Mielczarek, and Kuyatt [53] for reasons that are not clear.

C. Comparison of FOMBT results with experiment for the sum of the $3\,^1P$, $3\,^1D$, and $3\,^3D$ DCS's

Table V gives the FOMBT results for the electron-impact excitation DCS's of the $3\,^1P$, $3\,^1D$, and $3\,^3D$ levels of helium, as well as their sum. Figures 7 and 8 compare the FOMBT results with the available experimental data (Table II) for the sum of the DCS's for the excitation of the $3\,^1P$, $3\,^1D$, and $3\,^3D$ levels and also show the individual contributions from each of the three levels predicted by FOMBT. The first-order Born-approximation DCS for excitation of the $3\,^1P$ level is also shown to provide a perspective as to the effects of distortion and exchange in altering both the shape and magnitude of the DCS. At all energies studied, the FOMBT results are in quantitative agreement with experiment except for 50-eV incident electron energy and $50° \leq \theta \leq 100°$ angles. At lower energies ($\leq$40 eV) and higher angles ($\theta \geq 50°$), there is a substantial contribution from excitation of $3\,^1D$ and $3\,^3D$ levels, but at higher energies ($\geq$50 eV) the summed DCS is essentially identical to the $3\,^1P$ DCS (see Table V). At 100-eV incident electron energy, the agreement between FOMBT and experiment is excellent. To our knowledge, there are no other experimental data to which a comparison can be made.

Figure 9 shows a comparison of the DCS's obtained from our FOMBT calculations for excitation of the $3\,^1P$ level with the available experimental data [36] and theoretical results from the DWA [42,43], the distorted-wave polarized orbital (DWPO) [48], and multichannel-eikonal (MCE) [54] approximations, at 81.6 and 100 eV. As this comparison shows, the results from FOMBT and

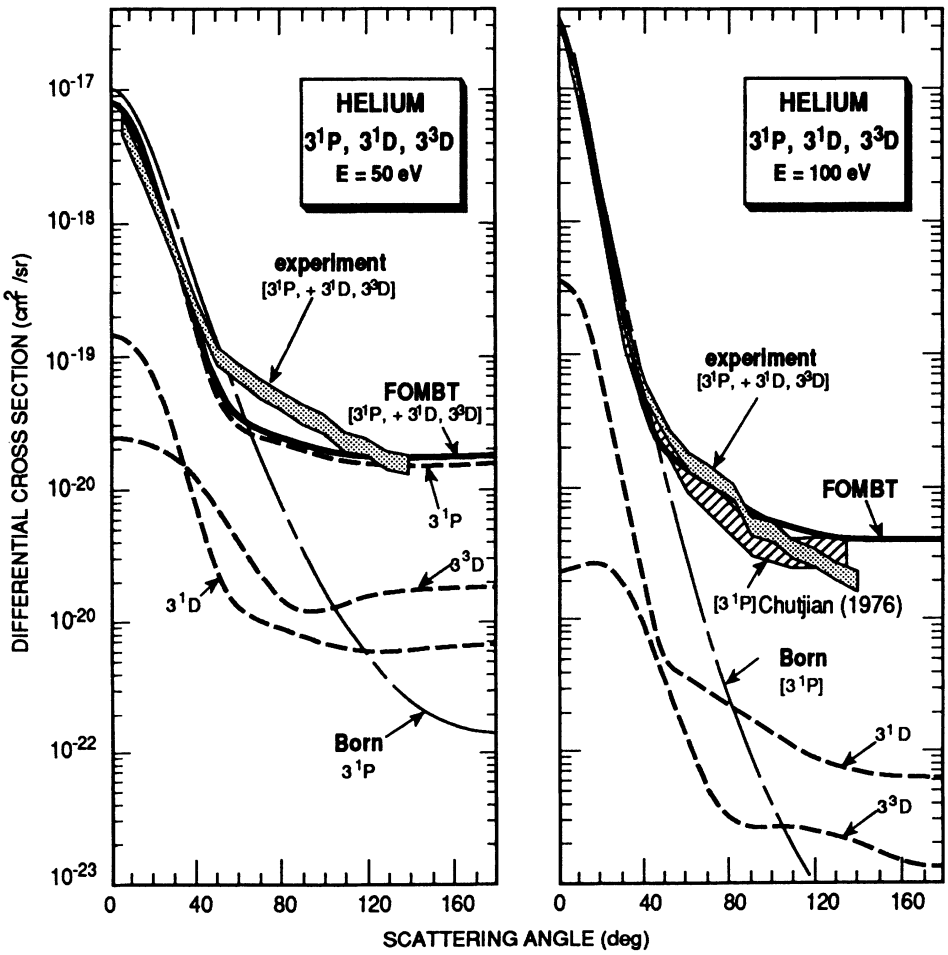

FIG. 8. Same as Fig. 7, except for $E=50$ eV (left panel) and $E=100$ eV (right panel) incident electron energies. Present experimental results are shown and those obtained by renormalizing the results of Chutjian [36]. (See Table II.)

the DWA agree reasonably well with experimental data which are substantially larger than the DCS results obtained from the DWPO and MCE calculations. The MCE approximation is deficient because exchange is not included in the model and this omission is responsible for a predicted DCS that is too small at intermediate and large scattering angles.

D. Integral cross sections for the excitation of $2\,^1P$, $3\,^1P$, and $4\,^1P$ levels

In Table VI the present experimental ICS's for excitation of the $2\,^1P$ and $3\,^1P$ levels are compared with those obtained from optical excitation functions corrected for cascade by Westerveld, Heideman, and Van Eck [17], Shemansky *et al.* [18], and with results from our FOMBT calculation. The agreement between the optical and the electron-scattering results and the experimental and theoretical results is quite good. Table VI also contains the ICS's for excitation of the $4\,^1P$, $5\,^1P$, and $6\,^1P$ levels, although there are no experimental data to which the FOMBT results can be compared for $n=5$ and 6.

The present experimental and FOMBT results for the ICS's in the case of $2\,^1P$, $3\,^1P$, and $4\,^1P$ excitations are compared with other experimental and theoretical results in Figs. 10 and 11, respectively. These figures show that FOMBT results agree well with the experimental ICS data in the $E > 100$-eV energy range and lie closer to the experimental data for all energies than the five-state R-matrix [23] and five-state close-coupling ICS results [46], which overestimate the cross section.

The comparison of various scattering models with experimental data in the case of the $1\,^1S \rightarrow 2\,^1P$ excitation has been discussed by Brandsen and McDowell [15], by Callaway [19], by Itikawa [21], and by Aggarwal, Kingston, and McDowell [56]. All these authors point out the excellent agreement of the FOMBT results with the experimental data even in the low-energy region. According to Callaway [19], the success of distorted-wave

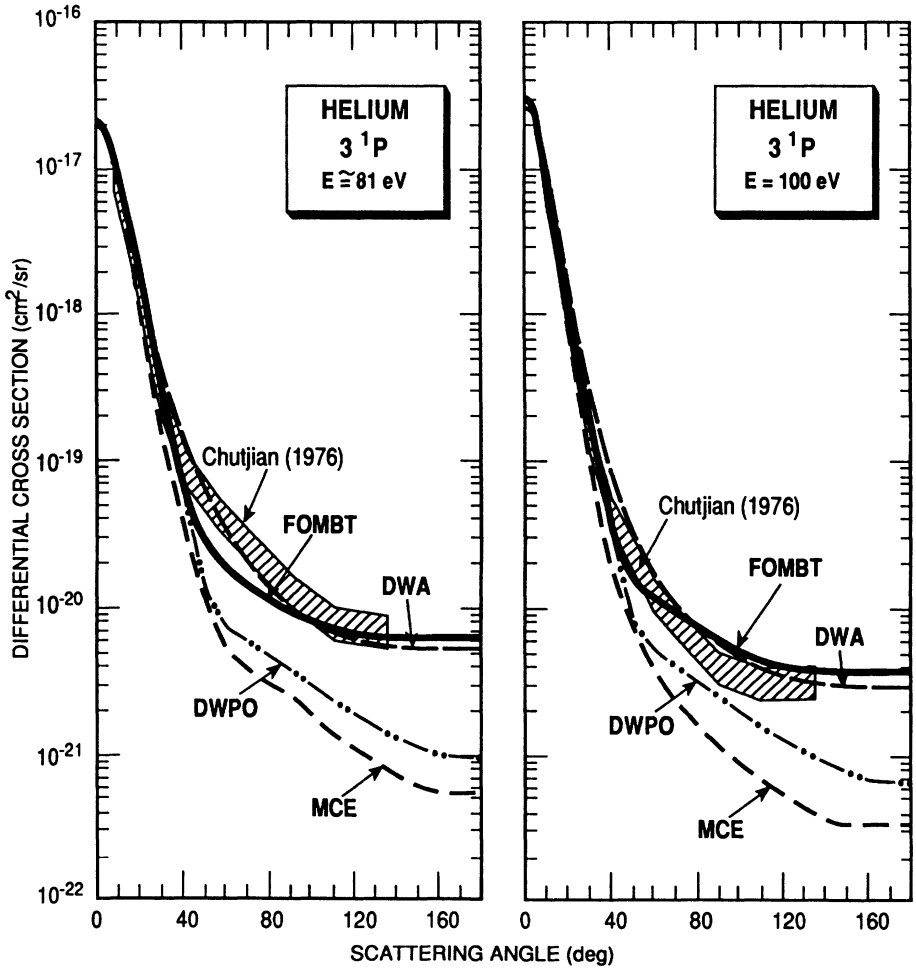

FIG. 9. Comparison of present FOMBT results with DCS's deduced from the experimental data of Chutjian [36] (see Table II) for excitation of the $3\,^1P$ level of helium, for $E \cong 81$ eV (left panel) and $E = 100$ eV (right panel), incident electron energies. The DWPO results of Scott and McDowell [48], the MCE theory results of Flannery and McCann [54], and the DWA results of Bartschat and Madison [42,43] are shown for comparison.

methods in the low-energy region was largely unexpected. In the high-energy region (i.e., for $E \geq 200$ eV), the DWA, DWPO, and MCE theories also give ICS results in good agreement with the experimental data. However, MCE and DWPO results for the DCS disagree markedly with the experimental data for scattering angles $\theta > 30°$, even for $E = 200$ eV incident electron energy, because of deficiencies in the scattering models employed.

The comparison of theoretical results with the experimental data in the case of the $3\,^1P$ excitation (Fig. 11) has been discussed by Bransden and McDowell [15]. Here again, in addition to FOMBT and DWA, the DWPO and MCE theory results show good agreement with the experimental ICS data for $E \geq 200$ eV energies. However, as can be seen from Fig. 9, at $E = 100$ eV electron energy, both DWPO and MCE give poor results for the DCS for $\theta > 45°$, as was the case for the $2\,^1P$ excitation.

The situation is similar for the $4\,^1P$ excitation, as shown in Fig. 11. A discussion of the comparison between DWPO and MCE theory results to experimental data was made by Bransden and McDowell [15].

E. Scaling laws for the excitation of $n\,^1P$ ($n = 2, 3, \ldots$) levels of He

Table VI contains the FOMBT results for the ICS for excitation of $n\,^1P$ ($n = 2, 3, \ldots, 6$) levels in helium. In an

TABLE VII. Energy dependence for the quantity $n^3\sigma\,(n\,^1P)$ (10^{-17} cm^2) for excitation of $n\,^1P$ levels ($n \geq 6$) of helium, as obtained from FOMBT and the first-order Born approximations, and the summed integral cross section (10^{-17} cm^2) for excitation of the $n\,^1P$ levels in helium.

	$n^3\sigma(n\,^1P)$		Sum $= \sum_{n=2}^{\infty} \sigma(n\,^1P)$
Energy (eV)	FOMBT	Born	FOMBT
25	0.164	2.279	0.163
27.5	0.439	4.555	0.325
30	1.198	5.854	0.506
35	2.616	7.387	0.844
40	3.877	8.208	1.111
50	5.599	8.871	1.450
60	6.489	8.960	1.607
70	6.906	8.789	1.673
81.6	7.085	8.497	1.685
100	7.003	7.970	1.647
150	6.255	6.690	1.450
200	5.499	5.748	1.269
300	4.409	4.519	1.014
400	3.689	3.752	0.847
500	3.184	3.223	0.730

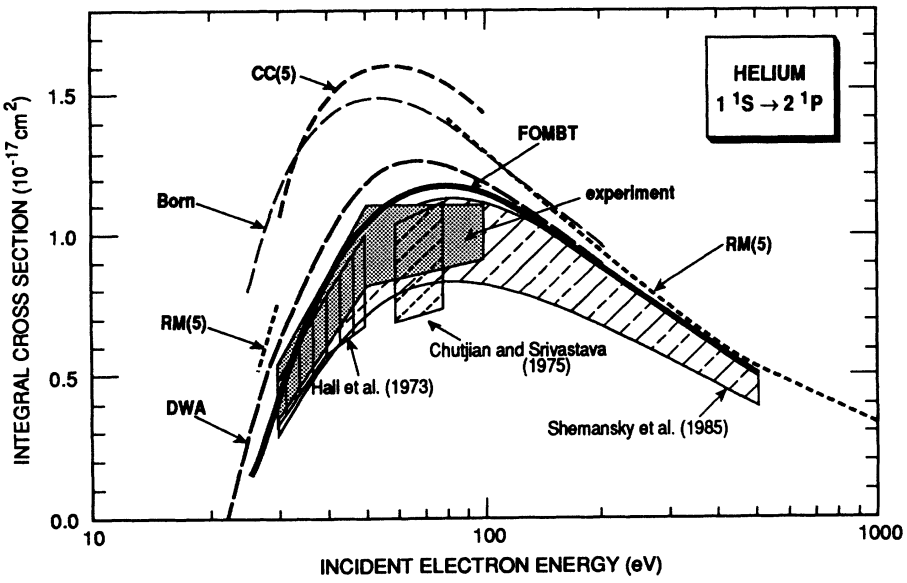

FIG. 10. Comparison of theoretical and experimental integral cross sections for excitation of the $2\,^1P$ level in helium. Theoretical results shown are the following: five-state close-coupling [CC(5)] calculation results of Bhadra, Callaway, and Henry [46], the first-order Born-approximation results of Bell, Kennedy, and Kingston [52], the five-state R-matrix [RM(5)] calculation results of Fon, Berrington, and Kingston [25], the distorted-wave-approximation (DWA) results of Madison and co-workers [41,43], and the present FOMBT results. The present results (experiment) are shown along with those of Chutjian and Srivastava [35], Hall *et al.* [47], and Shemansky *et al.* [18].

earlier publication [7], two of the present authors discussed a simple scaling law for the excitation of $n\,^1P$ ($n=2,3,\ldots$) levels of helium and stated there that, as has been known for many years, the ICS is expected to be (approximately) proportional to n^{-3} for $n\,^1P$ ($n \gtrsim 5$ or 6) excitation. The n^{-3} scaling of the $n\,^1P$ ICS's will also apply to those cross sections for excitation of the other symmetries in helium: ^1S, ^1D, ^3S, ^3P, and ^3D [29,57] because it is associated with final target-state normalization.

The quantity $n^3\sigma(n\,^1P)$ [where $\sigma(n\,^1P)$ denotes the ICS for excitation of a particular $n\,^1P$ level in helium] is shown in the upper panel in Fig. 12, as a function of the incident electron energy, for $n=2$–6. For $n \geq 6$, the quantity $n^3\sigma(n\,^1P)$ behaves according to the same function of the energy, independent of n, one for the FOMBT cross sections and a different one for the first-order Born approximation. These "asymptotic" (i.e., large n) functions are shown in the lower panel in Fig. 12 for the first-order Born approximation for FOMBT and are tabulated in columns 2 and 3 in Table VII.

The upper panel in Fig. 13 compares the sum of FOMBT integral cross sections

$$\mathcal{S} = \sum_{n=2}^{3 \text{ or } 4} \sigma(n\,^1P) ,$$

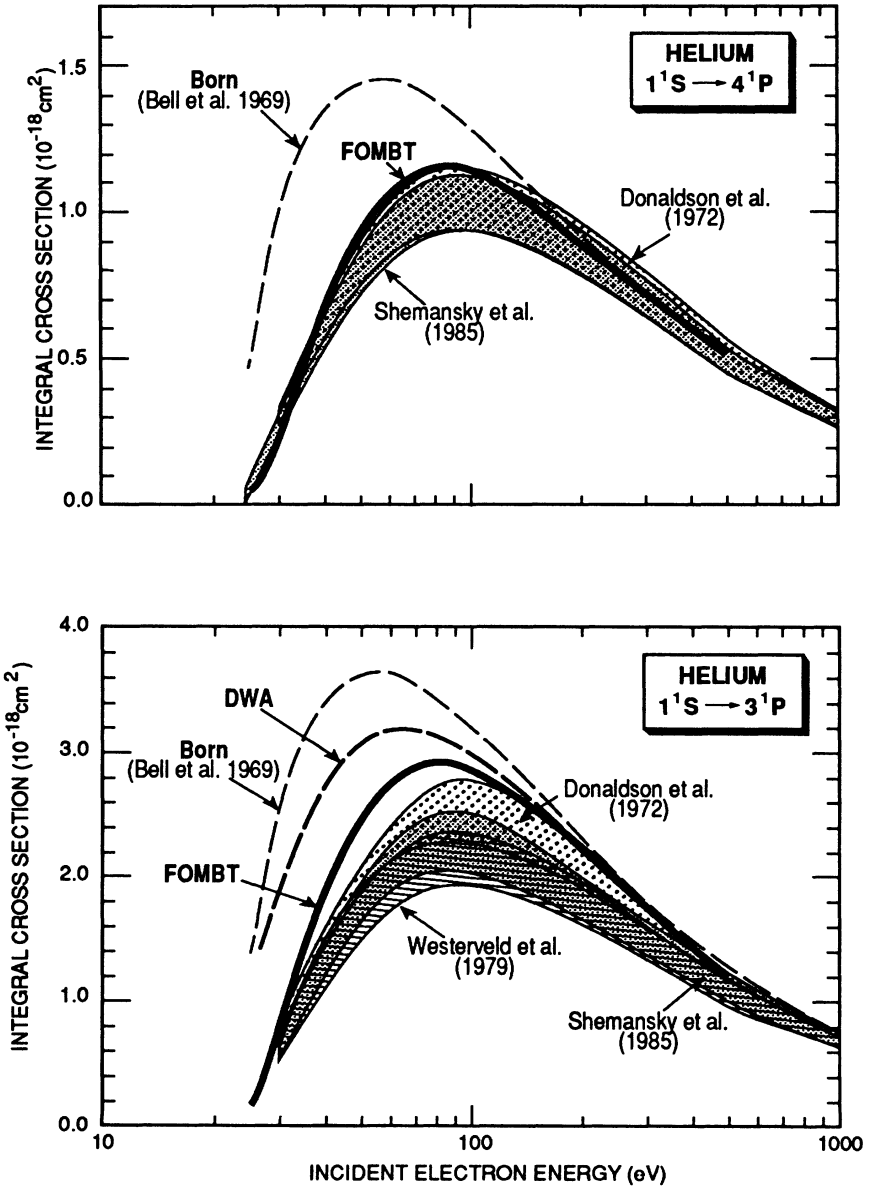

FIG. 11. Same as Fig. 10, except for the excitation of the $4\,^1P$ level (upper panel) and of the $3\,^1P$ level (lower panel). Theoretical results shown are the following: first-order-Born approximation results of Bell, Kennedy, and Kingston [52], distorted-wave approximation (DWA) results of Bartschat and Madison [42,43], and the present FOMBT results. Experimental results shown are from Shemansky *et al.* [18], Donaldson, Hender, and McConkey [55], and Westerveld, Heideman, and van Eck [17].

as a function of the number of levels taken in the above sum, with results reported by Shemansky *et al.* [18]. The values predicted by FOMBT are seen to be about 20% larger than those estimated by Shemansky *et al.* [18]. The lower panel in Fig. 13 shows the plot of $\sum_{n=2}^{x}\sigma(n\,^1P)$ as a function of incident electron energy for $x=2,\ldots,5$, and ∞. The sum over n of the FOMBT ICS's can be easily evaluated by using the second column in Table VII, the n^{-3} dependence of the integral cross section (for $n\geq 6$), and the fact [58] that $\sum_{n=1}^{\infty}n^{-3}=1.2020569$. That sum, over all FOMBT $n\,^1P$ ICS's as a function of incident electron energy, is also given in the last column in Table VII.

Using the excitation cross sections obtained from our FOMBT calculations for excitation of the $n\,^1P$ level given here, plus the corresponding results for the excitation of the other five final-state target symmetries [57], along with the n^{-3} scaling for $n\geq 6$ a "total" integral excitation cross section (that is, to all the bound states) for helium (i.e., $\sum_{n=2\ (\text{or}\ 3)}^{\infty}\sigma_n$) can be derived [29,57]. This "total" excitation cross section involves excitation to the six final-state symmetries in helium: ^3S, ^1S, ^3P, ^1P, ^3D, ^1D (neglecting F and higher-L states), a discussion of which is beyond the scope of this paper. This analysis will be

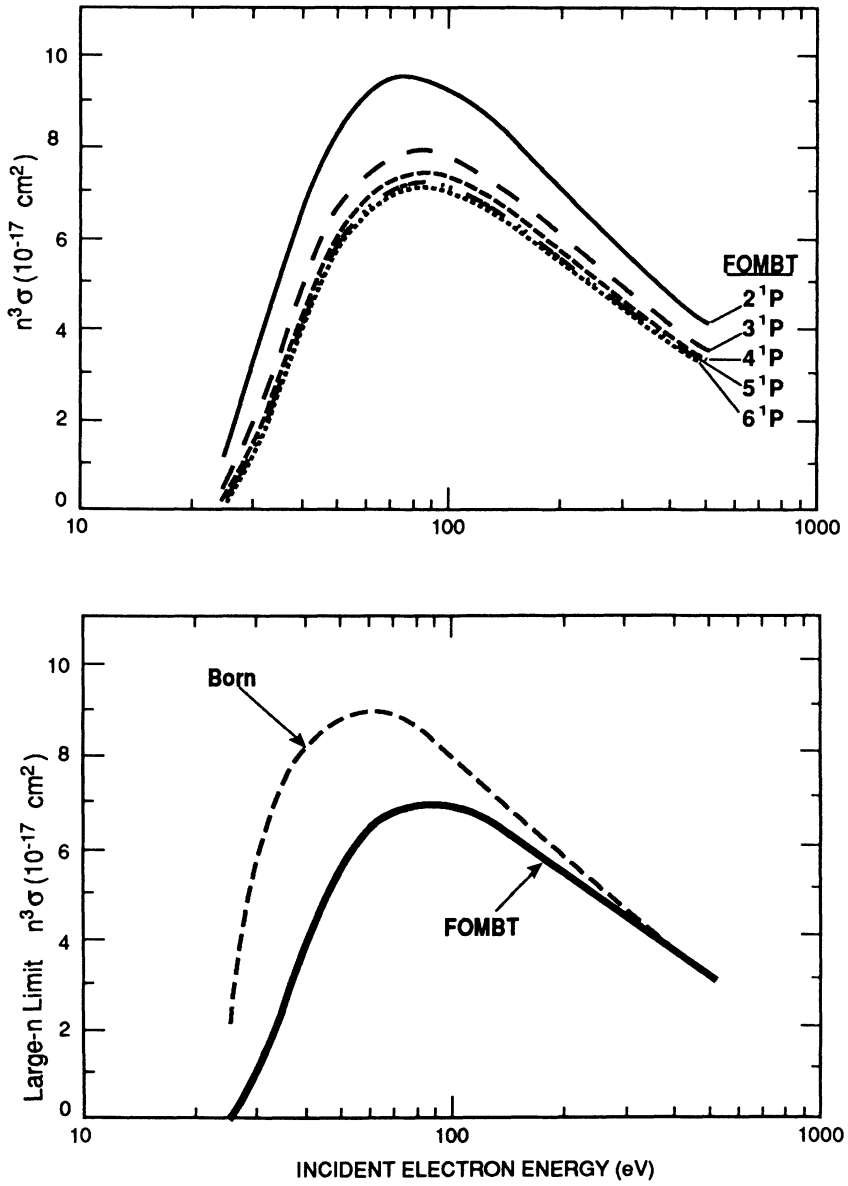

FIG. 12. (Upper panel) Principal quantum number cubed (n^3) times the integral cross section (σ) for excitation of the $n\,^1P$ ($n=2,\ldots,6$) levels in helium, as a function of the incident electron energy. The results in this figure show that n^3 times the integral cross section becomes independent of n for $n\gtrsim 6$. (Lower panel) Converged large-n limit for n^3 times the integral cross section, for both the Born and FOMBT approximations, as a function of incident electron energy. The values plotted are also given in Table VII and can be used to determine the DCS and ICS for excitation of any $n\,^1P$ ($n\geq 6$) level of helium by dividing the entries by the appropriate value of n^3.

reported in detail in Refs. [29] and [57] so only the final results will be presented here. The upper panel in Fig. 14 illustrates the individual contributions [29,57] to the total integral excitation cross section by each of the six symmetries, obtained by the above method, and shows that the largest contributions come from excitation of the $n\,^1P$, $n\,^1S$, and $n\,^3P$ levels for electron energies less than about 100 eV.

The lower panel in Fig. 14 compares this total integral excitation cross section predicted by FOMBT for helium with that deduced from experimental data according [29,57] to the formula

$$Q_{\text{tot exc}} = Q_{\text{tot scatt}} - Q_{\text{el scatt}} - Q_{\text{ion}} ,$$

where $Q_{\text{tot scatt}}$ refers to the total ICS, $Q_{\text{el scatt}}$ refers to the total elastic scattering ICS, and Q_{ion} refers to the total ionization ICS. Experimental results for $Q_{\text{tot scatt}}$, $Q_{\text{el scatt}}$, and Q_{ion} were obtained from Refs. [59], [60], and [61], respectively.

The comparison in the lower panel in Fig. 14 shows that total integral excitation cross sections predicted by FOMBT agrees within an assumed 10% error associated with the corresponding cross section deduced from experiment. Although this superb agreement between theory and experiment shown in Fig. 14 is probably somewhat fortuitous for the magnitude, we believe that the *shape* is a manifestation of the physics in the FOMBT and that both the relative and absolute contributions by the

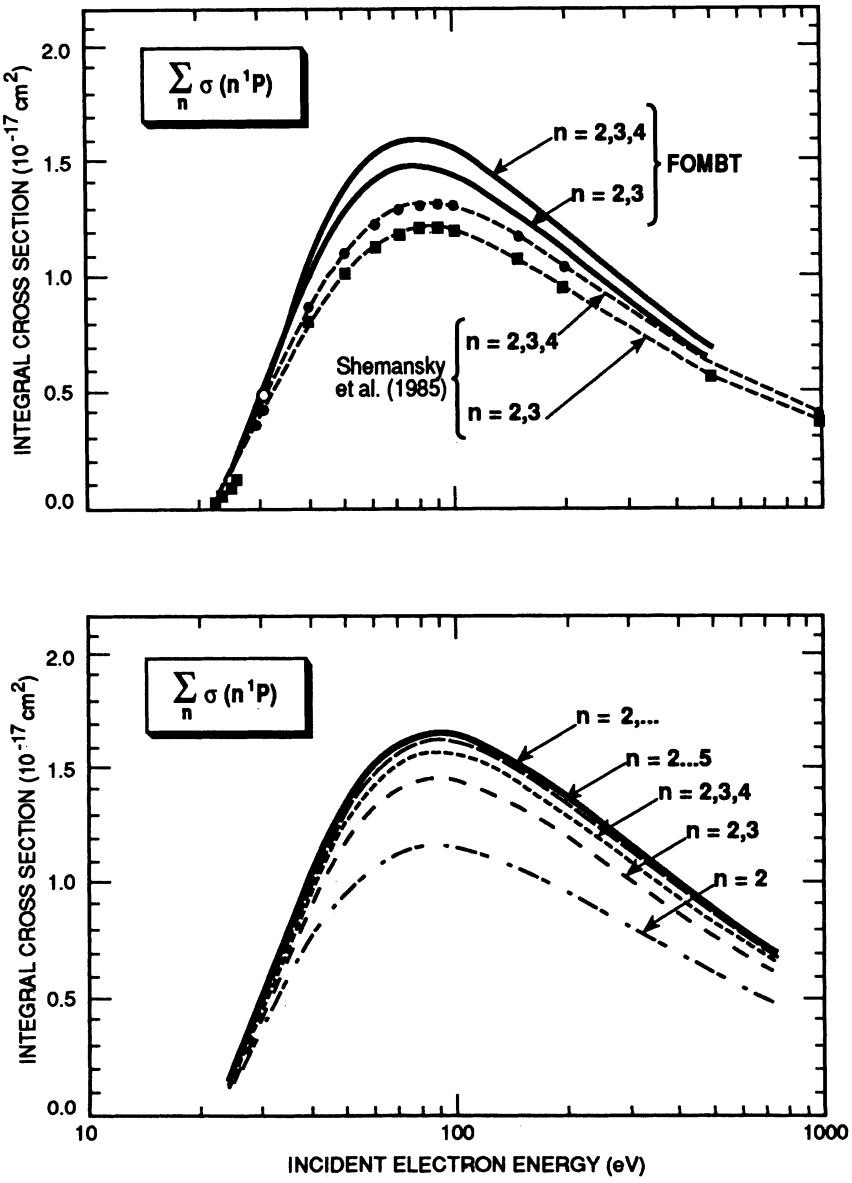

FIG. 13. (Upper panel) Comparison of $\sum_n \sigma(n\,^1P)$ obtained from FOMBT with that obtained by Shemansky *et al.* [18], as a function of the incident electron energy, for summing over $n=2,3$ and $n=2,3,4$. (Lower panel) $\sum_n \sigma(n\,^1P)$ for excitation of $n\,^1P$, predicted by FOMBT, as a function of the incident electron energy, from $n=2$ to ∞. This total cross section for direct excitation of all ^1P states in helium is also tabulated in the last column in Table VII.

different symmetries are accurately predicted by FOMBT.

V. CONCLUSIONS

In this work we report new experimental results for the electron-impact excitation of the $2\,^1P$ and of the unresolved $3\,^1P$, $3\,^1D$, and $3\,^3D$ levels of helium, as well as FOMBT results for excitation of the $n\,^1P$ ($n=2,3,\ldots 6$) levels of helium. The present work, in conjunction with earlier studies [7,8, 26–28] provides a comprehensive picture that substantiates the validity of FOMBT for treating excitation of $n\,^1P$ ($n=2,3,\ldots,6$) levels in helium with respect to DCS's, ICS's, and electron-impact coherence parameters. The FOMBT results agree nearly quantitatively with experiment for the energy and angular ranges studied here. One conclusion from this study is that FOMBT provides an accurate physical description of the electron-impact excitation process of the $n\,^1P$ ($n=2,3,\ldots$) levels for $E \geq 50$ eV incident electron energies. The scaling laws studied here also provide a very useful and reliable method for obtaining integral and

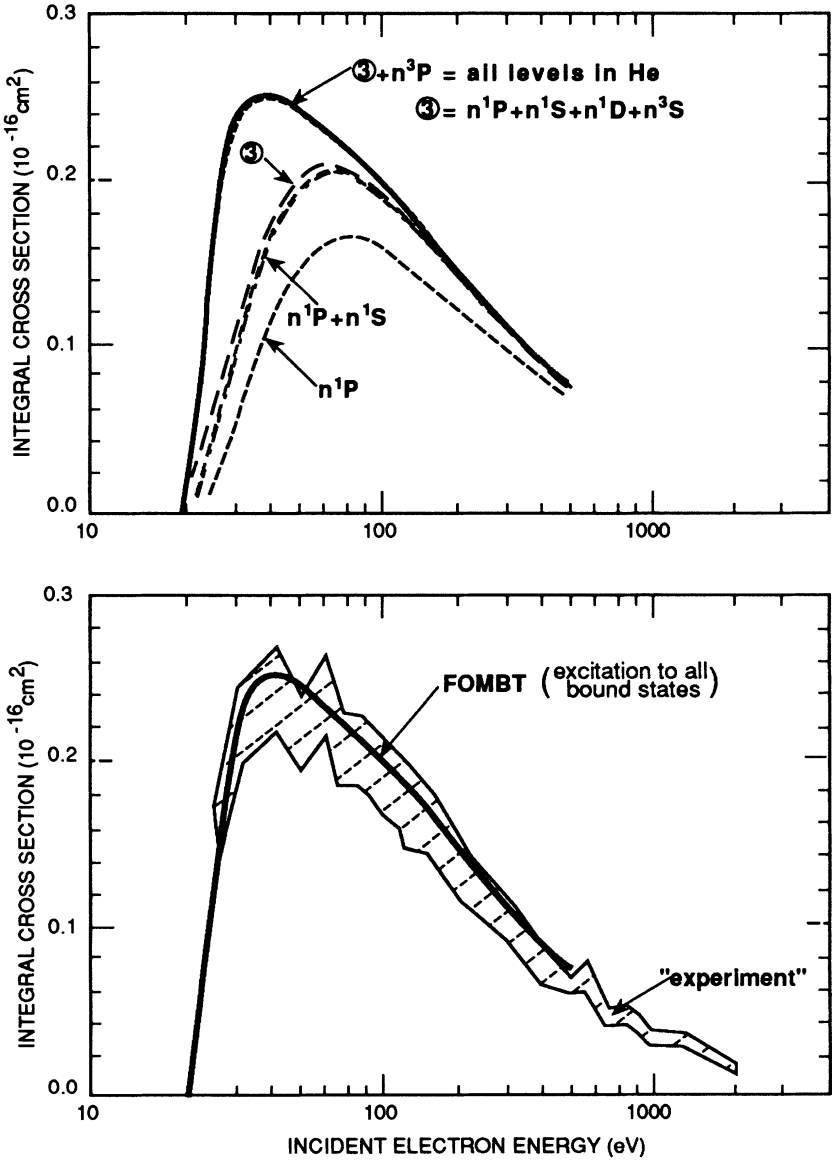

FIG. 14. (Upper panel) Various sums of the integral cross sections for electron-impact excitation of helium calculated using FOMBT, as a function of the electron-impact energy. The lowest curve denotes $\sum_{n=2}^{\infty}[\sigma(n\,^1P)]$; the next lowest curve is $\sum_{n=2}^{\infty}[\sigma(n\,^1P)+\sigma(n\,^1S)]$; the curve denoted by "3' represents $\sum_{n=2}^{\infty}[\sigma(n\,^1P)+\sigma(n\,^1S)+\sigma(n\,^1D)+\sigma(n\,^3S)]$, etc., to the highest-lying curve, and denotes the "total" excitation cross section (from the helium ground state), and represents the sum $\sum_{n=2\text{ or }3}^{\infty}[\sigma(n\,^1P)+\sigma(n\,^1S)+\sigma(n\,^1D)+\sigma(n\,^3S)+\sigma(n\,^3P)+\sigma(n\,^3D)]$. The extrapolation to $n=\infty$ was accomplished by using the n^{-3} scaling described in the text. (Lower panel) Comparison of the total excitation cross section for helium obtained from our FOMBT calculation with the corresponding "experimental" value obtained by subtracting the measured elastic-scattering and ionization cross sections from the measured total electron-scattering cross section in helium. See text for details.

differential cross sections for excitation of the higher ($n \geq 6$) lying $n\,^1P$ levels in helium. Although not yet tested, this characteristic is expected to apply to other atoms, such as neon, argon, and krypton, which will prove to be an asset for those involved in modeling rare-gas plasmas.

The results reported here suggest a number of additional experimental and theoretical investigations on helium, two of which are:

(a) Extend the measured angular distributions to larger scattering angles. The results in Figs. 2–4 show that available theories disagree most strongly for scattering angles greater than $\sim 90°$. Experimental data at larger angles would help determine which scattering model better describes the collision process.

(b) Use improved energy resolution or coincidence technique to resolve the $n=3$ manifold ($3\,^1P, 3\,^1D, 3\,^3D$) and obtain DCS's for excitation of individual levels. Such experimental data would enable a test of the n^{-3} scaling predicted here for $n\,^1P$ and a direct comparison of the predicted and measured DCS's for excitation of the $3\,^1D$ and $3\,^3D$ levels.

ACKNOWLEDGMENTS

David C. Cartwright and George Csanak gratefully acknowledge the financial support of the U.S. DOE, the NSF (OIP), and the University of California (Riverside)—Los Alamos National Laboratory Collaborative Research Program (CALCOR) for supporting this research. Partial support to S.T. at JPL, CalTech by NASA is acknowledged. The authors thank Professor Don Madison (University of Missouri) for providing his results (Ref. [43]) in tabulated form.

*Present address: Phillips Petroleum Co., Bartlesville, OK 74003.

[1] H. S. W. Massey and C. B. O. Mohr, Proc. R. Soc. London **132**, 605 (1931).
[2] W. Hanle, Z. Phys. **56**, 94 (1929).
[3] E. G. Dymond and E. E. Watson, Proc. R. Soc. London Ser. A **122**, 571 (1929); J. H. McMillen, Phys. Rev. **36**, 1034 (1930).
[4] C. B. O. Mohr and F. H. Nicoll, Proc. R. Soc. London Ser. A **138**, 229 (1932).
[5] H. S. W. Massey and C. B. O. Mohr, Proc. R. Soc. London Ser. A **139**, 187 (1933).
[6] H. S. W. Massey and C. B. O. Mohr, Proc. R. Soc. London Ser. A **140**, 613 (1933).
[7] G. Csanak and D. C. Cartwright, Phys. Rev. A **34**, 93 (1986).
[8] G. Csanak and D. C. Cartwright, Phys. Rev. A **38**, 2740 (1988).
[9] D. R. Bates, A. Fundaminsky, and H. S. W. Massey, Philos. Trans. R. Soc. London Ser. A **243**, 1950.
[10] D. R. Bates, A. Fundaminsky, J. W. Leech, and H. S. W. Massey, Philos. Trans. R. Soc. London Ser. A **243**, 117 (1950).
[11] Y. K. Kim and M. Inokuti, Phys. Rev. **175**, 176 (1968).
[12] D. G. Truhlar, J. K. Rice, A. Kuppermann, S. Trajmar, and D. C. Cartwright, Phys. Rev. A **1**, 778 (1970).
[13] D. H. Madison and W. N. Shelton, Phys. Rev. A **7**, 499 (1973).
[14] B. H. Bransden and M. R. C. McDowell, Phys. R. **30**, 207 (1977).
[15] B. H. Bransden and M. R. C. McDowell, Phys. R. **46**, 249 (1978).
[16] M. J. Brunger, I. E. McCarthy, K. Ratnavelu, P. J. O. Teubner, A. M. Weigold, Y. Zhou, and L. J. Allen, J. Phys. B **23**, 1325 (1990).
[17] W. B. Westerveld, H. G. M. Heideman, and J. van Eck, J. Phys. B **12**, 115 (1979).
[18] D. E. Shemansky, J. M. Ajello, D. T. Hall, and B. Franklin, Astrophys. J. **296**, 774 (1985).
[19] J. Callaway, Adv. Phys. **29**, 771 (1980).
[20] H. R. J. Walters, Phys. Rep. **116**, 1 (1984).
[21] Y. Itikawa, Phys. Rep. **143**, 69 (1986).
[22] I. I. Fabrikant, O. B. Shpenik, A. V. Snegursky, and A. N. Zavilopulo, Phys. Rep. **159**, 1 (1988).
[23] W. C. Fon, K. A. Berrington, and A. E. Kingston, J. Phys. B **13**, 2309 (1980).
[24] L. C. G. Freitas, K. A. Berrington, P. G. Burke, A. E. Kingston, and A. L. Sinfailam, J. Phys. B **17**, L303 (1984); K. A. Berrington, P. G. Burke, L. C. G. Freitas, and A. E. Kingston, J. Phys. B **18**, 4135 (1985).
[25] W. C. Fon, K. A. Berrington, and A. E. Kingston, J. Phys. B **21**, 2961 (1988).
[26] G. D. Meneses and G. Csanak, Z. Phys. D **8**, 219 (1988).
[27] L. D. Thomas, B. S. Yarlagadda, H. S. Taylor, and G. Csanak, J. Phys. B **7**, 1719 (1974).
[28] A. Chutjian and L. D. Thomas, Phys. Rev. A **11**, 1583 (1975).
[29] (a) G. Csanak, D. C. Cartwright, and S. Trajmer, following paper, Phys. Rev. A **45**, 1625 (1992); (b) S. Trajmar, D. F. Register, D. C. Cartwright, and G. Csanak (unpublished).
[30] D. F. Register, S. Trajmar, and S. K. Srivastava, Phys. Rev. A **21**, 1134 (1980).
[31] S. W. Jensen, Ph.D. thesis, University of California, Riverside, 1978 (unpublished).
[32] S. Trajmar and D. F. Register, in *Electron Molecule Collisions,* edited by K. Takayanagi and I. Shimamura (Plenum, New York, 1984), pp. 427–493.
[33] D. F. Register, S. Trajmar, G. Steffensen, and D. C. Cartwright, Phys. Rev. A **29**, 1973 (1984).
[34] A. Chutjian, Rev. Sci. Instrum. **50**, 347 (1979).
[35] A. Chutjian and S. K. Srivastava, J. Phys. B **8**, 2360 (1975).
[36] A. Chutjian, J. Phys. B **9**, 1749 (1976).
[37] G. Csanak, H. S. Taylor, and R. Yaris, Phys. Rev. A **3**, 1322 (1971).
[38] T. N. Rescigno, C. W. McCurdy, and V. McKoy, J. Phys. B **7**, 2396 (1974).
[39] R. D. Cowan, J. Opt. Soc. Am. **58**, 808 (1968); **58**, 924 (1968).
[40] A. R. Edmonds, *Angular Momentum in Quantum Mechanics* (Princeton University Press, Princeton, NJ, 1960), pp. 37–45.
[41] D. H. Madison, J. Phys. B **12**, 3399 (1979); D. H. Madison and K. H. Winters, *ibid.* **16**, 4437 (1983).

[42] K. Bartschat and D. H. Madison, J. Phys. B **21**, 153 (1988).
[43] D. H. Madison (private communication).
[44] E. J. Mansky and M. R. Flannery, J. Phys. B **23**, 3987 (1990).
[45] A. Chutjian, R. Hippler, I. McGregor, and H. Kleinpoppen, *Abstracts of Contributed Reports, Eleventh International Conference on the Physics of Electronic and Atomic Collisions, Kyoto, 1979,* edited by K. Takayanagi and N. Oder (The Society for Atomic Collisions Research, Kyoto, 1979), p. 172.
[46] K. Bhadra, J. Callaway, and R. J. W. Henry, Phys. Rev. A **9**, 1841 (1979).
[47] R. I. Hall, G. Joyez, J. Mazeau, J. Reinhardt, and C. Scherman, J. Phys. (Paris) **34**, 827 (1973).
[48] T. Scott and M. R. C. McDowell, J. Phys. B **8**, 2369 (1975).
[49] M. D. Hidalgo and S. Geltman, J. Phys. B **5**, 617 (1972).
[50] L. Vriens, J. A. Simpson, and S. R. Mielczarek, Phys. Rev. **165**, 7 (1968).
[51] M. A. Dillon and E. N. Lassettre, J. Chem. Phys. **63**, 2373 (1975).
[52] K. L. Bell, D. J. Kennedy, and A. E. Kingston, J. Phys. B **2**, 26 (1969).
[53] G. E. Chamberlain, S. R. Mielczarek, and C. E. Kuyatt, Phys. Rev. A **2**, 1905 (1970).
[54] M. R. Flannery and K. J. McCann, J. Phys. B **8**, 1716 (1975).
[55] F. G. Donaldson, M. A. Hender, and J. W. McConkey, J. Phys. B **5**, 1192 (1972).
[56] K. M. Aggarwal, A. E. Kingston, and M. R. C. McDowell, Astrophys. J. **278**, 874 (1984).
[57] D. C. Cartwright, G. Csanak, and S. Trajmar, Phys. Rep. (to be published) 1992.
[58] *Handbook of Mathematical Functions,* edited by M. Abramowitz and I. A. Stegun, Natl. Bur. Stand. (U.S.) Appl. Math. Ser. No. **55** (U.S. GPO, Washington, D.C., 1964), pp. 807–811.
[59] J. C. Nickel, K. Imre, D. F. Register, and S. Trajmar, J. Phys. B **18**, 125 (1985).
[60] I. Shimamura, Sci. Papers Inst. Phys. Chem. Res. **82**, 1 (1989).
[61] M. B. Shah, D. S. Elliott, P. McCallion, and H. B. Gilbody, J. Phys. B **21**, 2751 (1988).

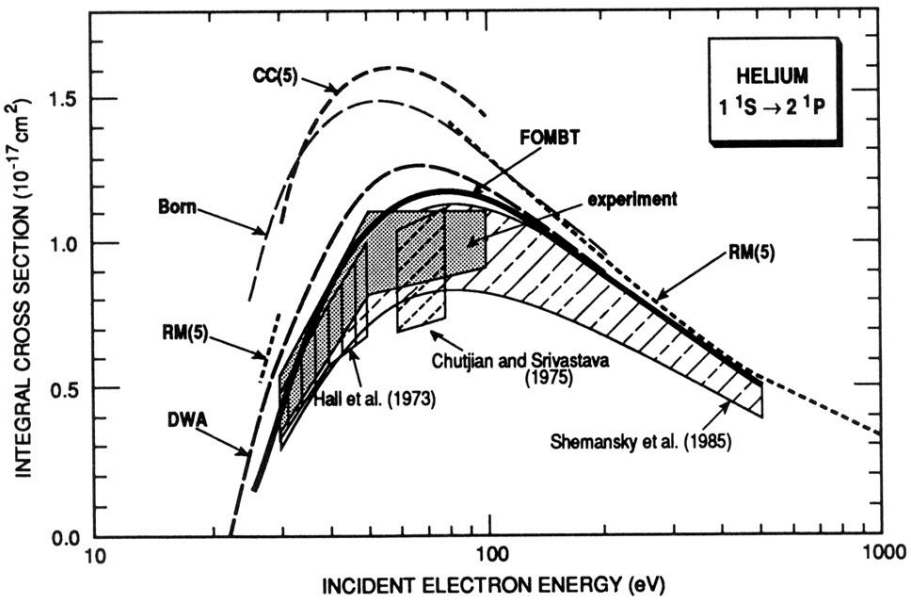

FIG. 10. Comparison of theoretical and experimental integral cross sections for excitation of the $2\,^1P$ level in helium. Theoretical results shown are the following: five-state close-coupling [CC(5)] calculation results of Bhadra, Callaway, and Henry [46], the first-order Born-approximation results of Bell, Kennedy, and Kingston [52], the five-state R-matrix [RM(5)] calculation results of Fon, Berrington, and Kingston [25], the distorted-wave-approximation (DWA) results of Madison and co-workers [41,43], and the present FOMBT results. The present results (experiment) are shown along with those of Chutjian and Srivastava [35], Hall *et al.* [47], and Shemansky *et al.* [18].

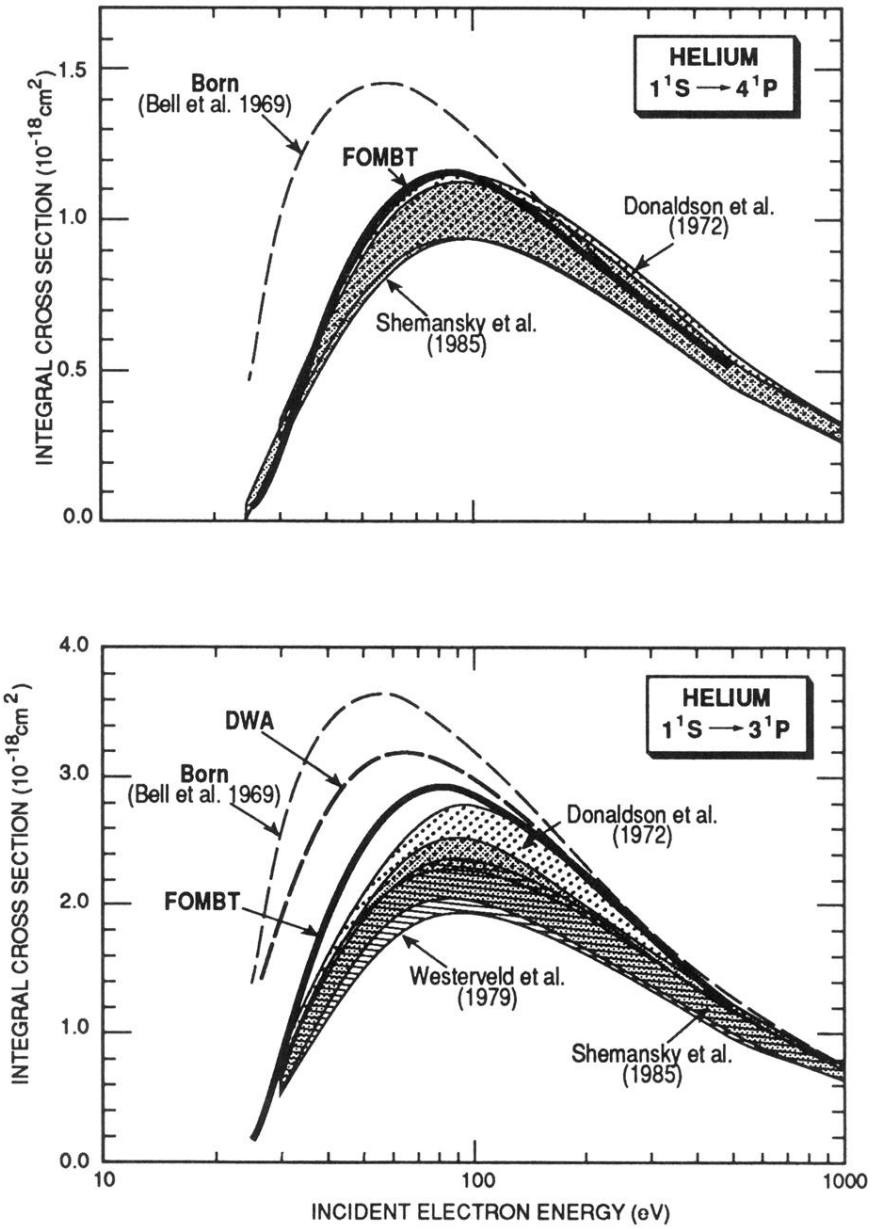

FIG. 11. Same as Fig. 10, except for the excitation of the $4\,^1P$ level (upper panel) and of the $3\,^1P$ level (lower panel). Theoretical results shown are the following: first-order-Born approximation results of Bell, Kennedy, and Kingston [52], distorted-wave approximation (DWA) results of Bartschat and Madison [42,43], and the present FOMBT results. Experimental results shown are from Shemansky *et al.* [18], Donaldson, Hender, and McConkey [55], and Westerveld, Heideman, and van Eck [17].

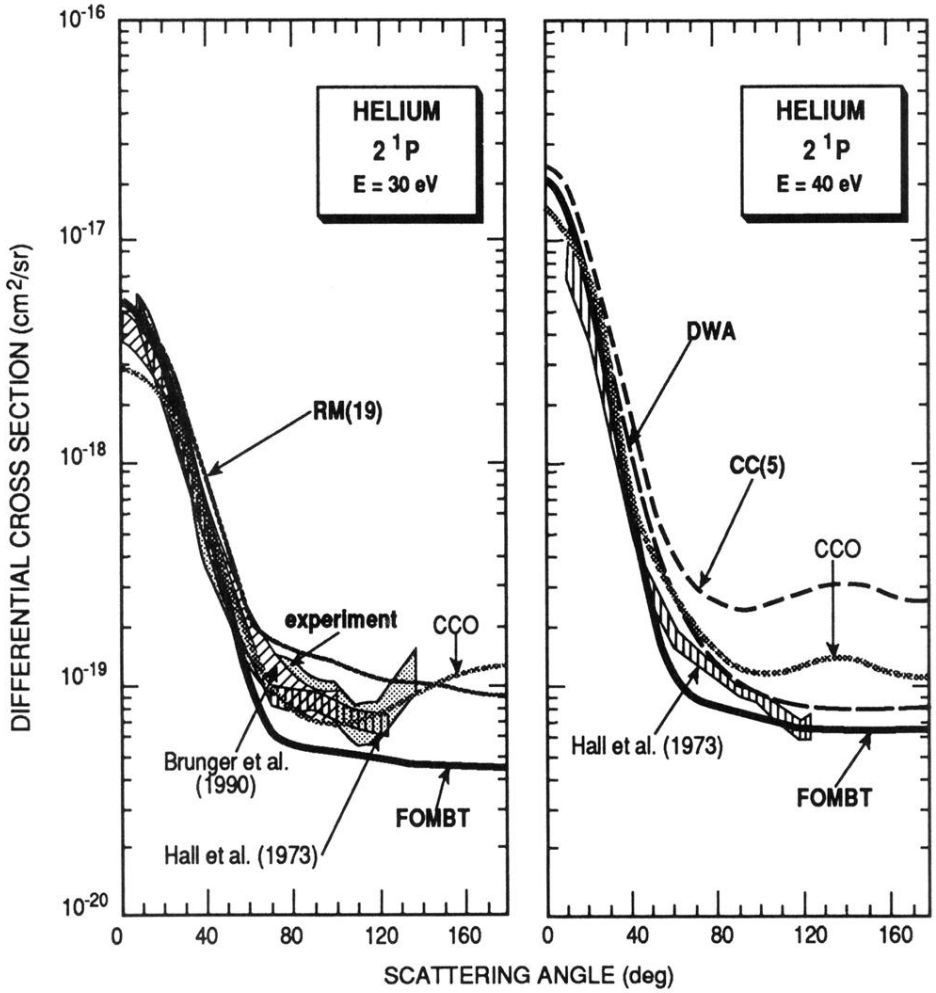

FIG. 2. Comparison of experimental and theoretical DCS's for excitation of the $2\,^1P$ level of helium, at 30 eV (left panel) and 40 eV (right panel) incident electron energies. Theoretical results shown in one or both panels include: the five-state close-coupling calculation results [CC(5)] of Bhadra, Callaway, and Henry [46], the 19-state R -matrix calculation results of Fon, Berrington, and Kingston [25] [RM(19)], results from the distorted-wave approximation (DWA) calculation of Madison and co-workers [41,43] ten-state coupled channels optical calculation (CCO) results of Brunger *et al.* [16], and the present FOMBT results. Experimental results shown are those of Hall *et al.* [47], Brunger *et al.* [16], and from the present study (experiment).

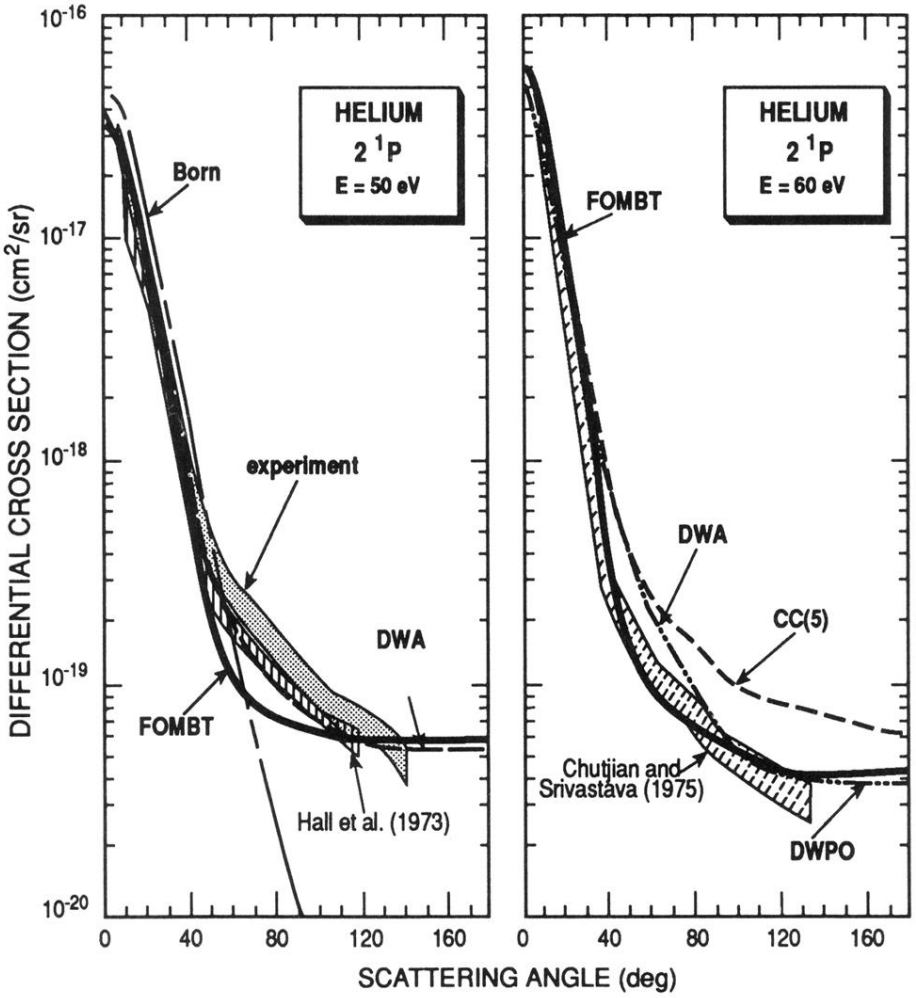

FIG. 3. Same as Fig. 2, except for 50-eV (left panel) and 60-eV (right panel) incident electron energies. Theoretical results shown are as follows: present FOMBT results, five-state close-coupling results of Bhadra, Callaway, and Henry [46] [CC(5)], the distorted-wave polarized orbital (DWPO) results of Scott and McDowell [48], and DWA results of Madison and co-workers [41,43]. The curve labeled Born denotes first-order Born-approximation results from the present study. The shaded areas represent experimental results (with their error limits) of Hall *et al.* [47], Chutjian and Srivastava [35] (renormalized), as well as the present measurements labeled "experiment."

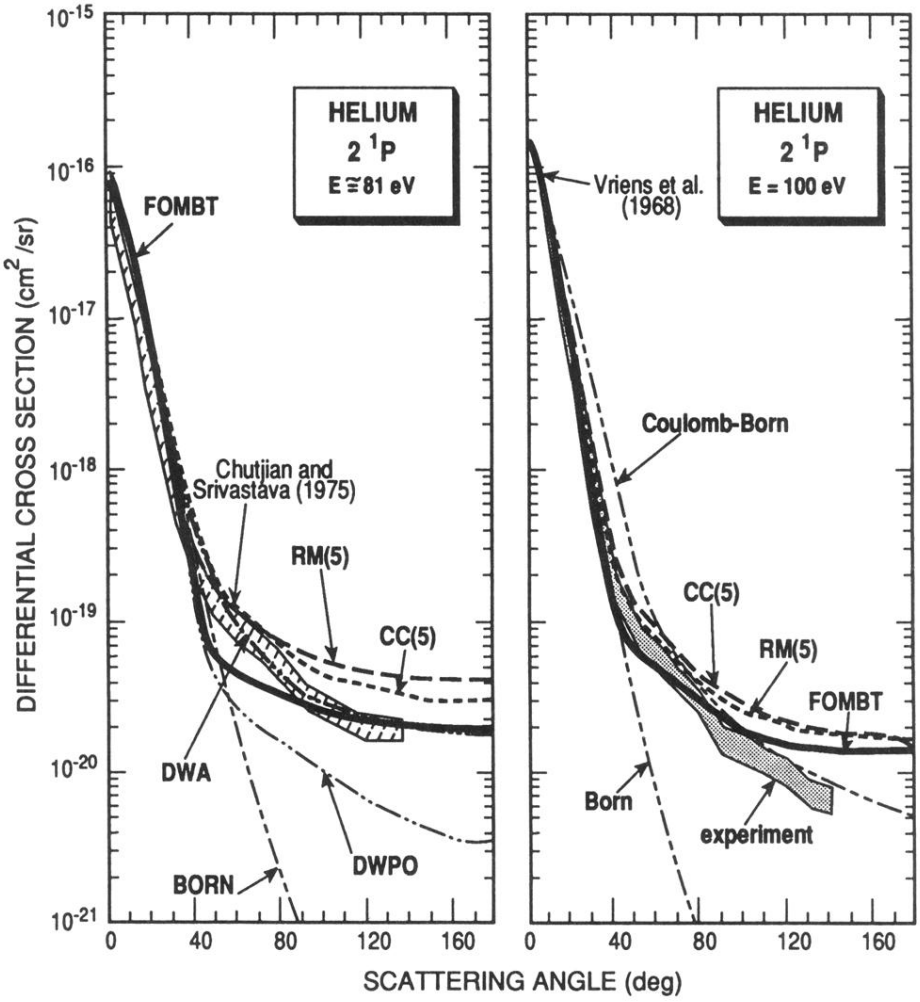

FIG. 4. Same as Fig. 2, except for $E \cong 81$ eV (left panel) and $E = 100$ eV (right panel) incident electron energies. Theoretical results, shown are as follows: present FOMBT results, five-state R-matrix results of Fon, Berrington, and Kingston [25] [RM(5)], five-state close-coupling results of Bhadra, Callaway, and Henry [46] [CC(45)], DWA results of Madison and co-workers [41,43], and DWPO results of Scott and McDowell [48]. The results of the present first-order Born approximation and those of the Coulomb-Born approximation of Hidalgo and Geltman [49] are also shown. The experimental results shown are from Chutjian and Srivastava [35] at 80 eV (renormalized), Vriens, Simpson, and Mielczarek [50], and present study at 100 eV, labeled "experiment".

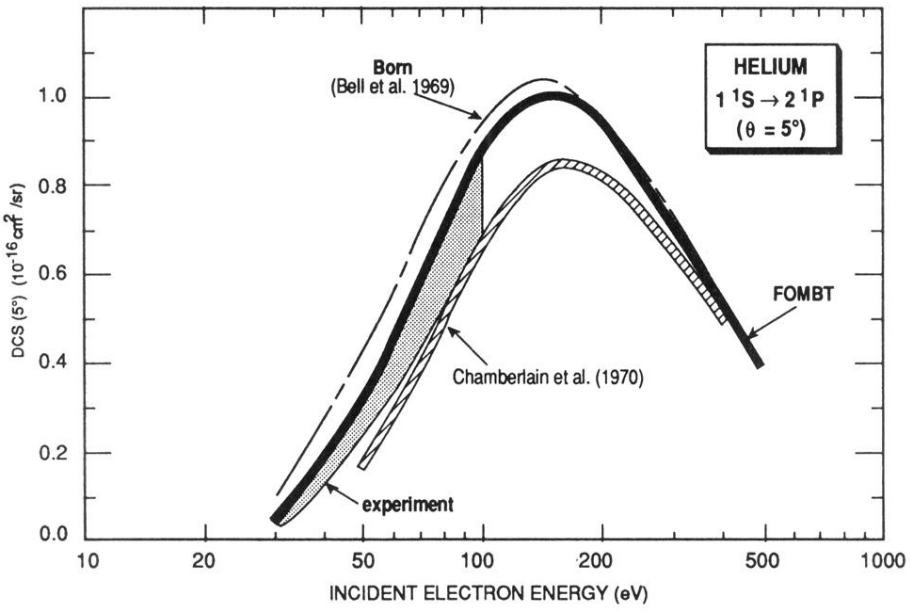

FIG. 6. Comparison of experimental and theoretical results for the dependence of the DCS ($\theta = 5°$) on the incident electron energy, for excitation of the $2\,^1P$ level in helium. The solid line denotes the FOMBT results, the dashed line is the first-order Born-approximation results of Bell, Kennedy, and Kingston [52]. The lightly shaded region denotes the present experimental results, and the earlier experimental results of Chamberlain, Mielczarek, and Kuyatt [53] are shown with cross hatching.

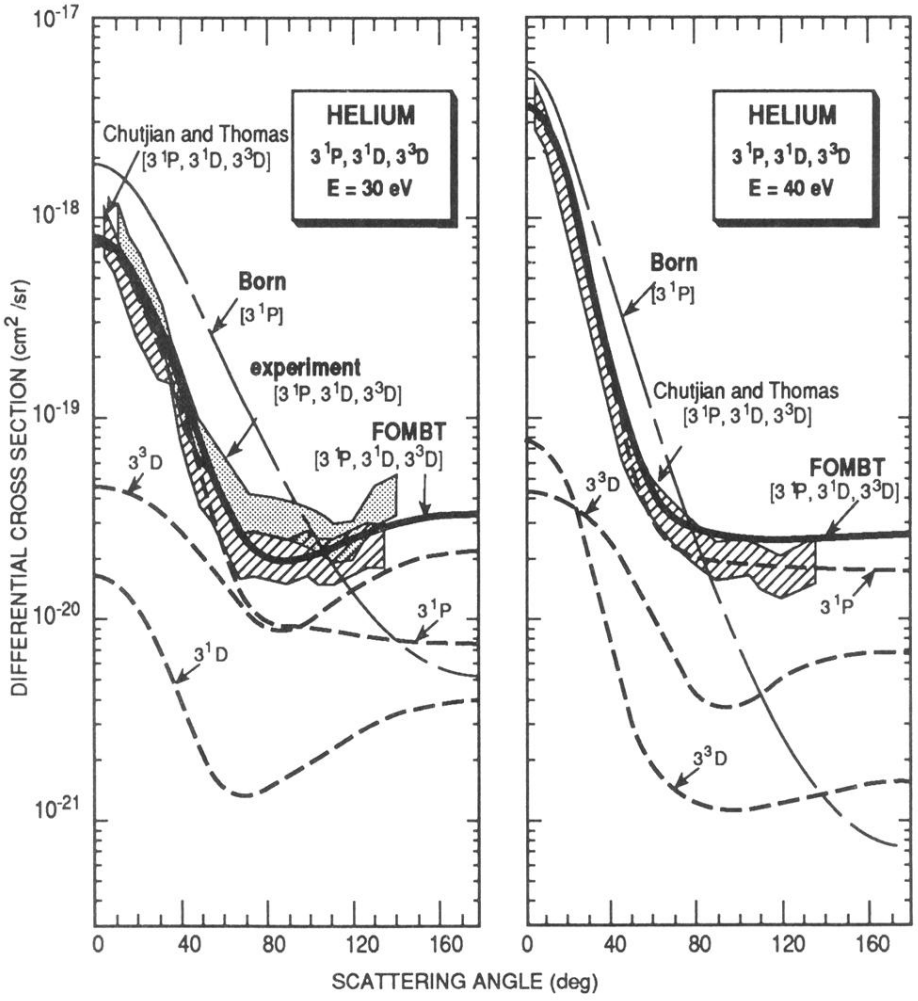

FIG. 7. Comparison of experimental and theoretical DCS's for excitation of the unresolved $3\,^1P, 3\,^1D, 3\,^3D$ levels of helium, at $E \cong 30$ eV (left panel) and $E = 40$ eV (right panel) incident electron energies. The solid line denotes the present FOMBT results for the sum of the three DCS's. The individual DCS's are shown by the appropriately labeled heavy dashed lines. The present first-order Born-approximation results for excitation of the $3\,^1P$ level are also shown. The shaded regions represent the present experimental results (left panel), and those of Chutjian and Thomas [28] (both panels).

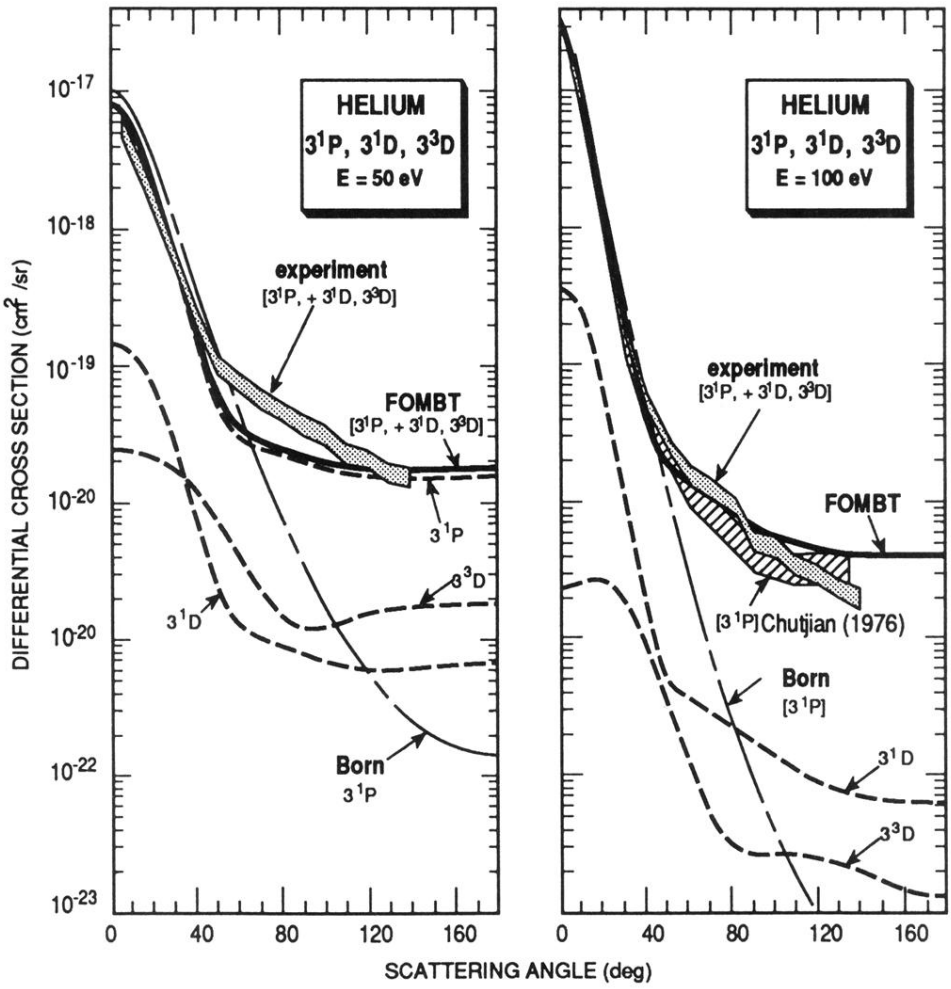

FIG. 8. Same as Fig. 7, except for $E = 50$ eV (left panel) and $E = 100$ eV (right panel) incident electron energies. Present experimental results are shown and those obtained by renormalizing the results of Chutjian [36]. (See Table II.)